ABSTRACT

HYDRODYNAMIC CFD MODELING OF A PHARMACEUTICAL REACTOR VESSEL PROVIDED WITH A RETREAT-BLADE IMPELLER UNDER DIFFERENT BAFFLING CONDITIONS

by
Christopher G Foehner

In the pharmaceutical industry, glass-lined reactors and vessels are often utilized to carry out a variety of different unit operations. Within these systems, both the vessel and impellers are typically glass-lined in order to provide superior corrosion resistance, prevent product contamination, and enhance cleanability. This approach, in turn, often requires the use of different, and sometimes sub-optimal, baffling conditions, which affect the hydrodynamics of the vessels and the reactor performance.

Computational Fluid Dynamics (CFD) is a computational tool that employs numerical methods and algorithms to discretize and numerically solve partial differential equations (PDEs) representing mass, energy, and momentum conservation equations for the purpose of analyzing fluid flow problems. In recent years, CFD has been used successfully to model hydrodynamically complex systems such as stirred mixing systems. A variety of computational approaches and models are implemented in the CFD code to do so, including single reference frame (SRF), multiple reference frame (MRF), and sliding mesh (SM) models, also possibly combined with Volume of Fluid (VOF) models.

In this study, a scaled-down version of a pharmaceutical glass-lined reactor vessel equipped with a retreat curve impeller (RCI) and a torispherical bottom is modeled using the CFD *COMSOL* software under a variety of setups, including variations in impeller speed, impeller clearance, and baffling conditions. Several modeling approaches are

used. The CFD simulations result in the prediction of the power dissipated by the impeller and therefore the impeller Power Number. These predictions are then compared with the experimental results obtained in previous work by this group.

In the fully baffled system, the values of the Power Numbers predicted by the simulations under turbulent conditions using MRF modeling are in close agreement with the experimental results across all tested impeller rotational speeds. In the partially baffled system, the results obtained with MRF modeling are very consistent with the experimental results. However, even better agreement is obtained when using the much more computationally expensive SM modeling technique. Finally, the simpler SRF approach proves to be very appropriate to model the unbaffled system, and good agreement between the simulation predictions and the experimental results is obtained, but only if the surface deformation of the liquid-air interface typically observed in unbaffled systems is small.

It can be concluded that the computational method used to simulate the hydrodynamic behavior of a pharmaceutical reactor vessel generates predictions that are in close agreement with experimental results, thus validating the CFD approach used to model this system.

HYDRODYNAMIC CFD MODELING OF A PHARMACEUTICAL REACTOR VESSEL PROVIDED WITH A RETREAT-BLADE IMPELLER UNDER DIFFERENT BAFFLING CONDITIONS

by
Christopher G Foehner

A Thesis
Submitted to the Faculty of
New Jersey Institute of Technology
in Partial Fulfillment of the Requirements for the Degree of
Master of Science in Biopharmaceutical Engineering

Otto H. York Department of
Chemical, Biological and Pharmaceutical Engineering

May 2014

APPROVAL PAGE

HYDRODYNAMIC CFD MODELING OF A PHARMACEUTICAL REACTOR VESSEL PROVIDED WITH A RETREAT-BLADE IMPELLER UNDER DIFFERENT BAFFLING CONDITIONS

Christopher G Foehner

Dr. Piero M. Armenante, Thesis Advisor Date
Distinguished Professor of Chemical, Biological and Pharmaceutical Engineering, NJIT

Dr. Robert B. Barat, Committee Member Date
Professor of Chemical, Biological and Pharmaceutical Engineering, NJIT

Dr. Laurent Simon, Committee Member Date
Associate Professor of Chemical, Biological and Pharmaceutical Engineering, NJIT

BIOGRAPHICAL SKETCH

Author: Christopher G Foehner

Degree: Master of Science

Date: May 2014

Undergraduate and Graduate Education:

- Master of Science in Biopharmaceutical Engineering,
  New Jersey Institute of Technology, Newark, NJ, 2014

- Bachelor of Arts in Economics-Mathematics,
  Columbia University, New York, NY, 2008

Major: Biopharmaceutical Engineering

Divide each difficulty into as many parts as is feasible and necessary to resolve it.
Rene Descartes

ACKNOWLEDGMENT

I would like to express my appreciation to my advisor, Dr. Piero Armenante, for his continuous support of my thesis and valuable feedback which made my research successful. His advice and recommendations were undoubtedly integral to the progression of my work. Thank you to Dr. Robert Barat and Dr. Laurent Simon for their participation as members of my thesis committee.

Also, I would like to recognize Bing Wang for providing some technical preparation to CFD software. Finally, I am forever indebted to my family and fiancé Romina Arceo for their extraordinary support of my academic endeavors and their constant encouragement. Thank you for everything you have given me.

TABLE OF CONTENTS

TABLE OF CONTENTS
(Continued)

Chapter **Page**

LIST OF TABLES

LIST OF FIGURES

LIST OF FIGURES
(Continued)

Figure **Page**

LIST OF SYMBOLS

H	Liquid height (mm)
T	Tank diameter (mm)
C_b	Impeller clearance measured from impeller bottom to tank bottom (mm)
Re	Reynolds Number
N_i	Agitation Rate (Hz)
μ	Dynamic fluid viscosity (Pa·s)
ρ	Fluid density (kg/m^3)
N_P	Newton Number (Power Number)
M	Torque (N·m)
P	Power (W)
F	Force (N)
m	Mass (kg)
a	Acceleration (m/s^2)
τ	Viscous surface forces (N)
f_x, f_y, f_z	Body forces (N)
u	Velocity (m/s)
D_i	Impeller diameter (m)
δ_{ij}	Kronecker delta (1,0)
k	Turbulent kinetic energy (m^2/s^2)
ε	Rate of dissipation of turbulent kinetic energy (m^2/s^3)
Fr	Froude Number

g	Acceleration due to gravity (m/s^2)
Q	Volumetric flow rate (m^3/s)
p	Pressure (Pa)
r	Radius (mm)
a	Length (mm)
h	Height (mm)
α	Central angle (deg)
c	Radius of ellipsoid (mm)

CHAPTER 1

INTRODUCTION

1.1 Background

Glass-lined, stirred reactors are frequently utilized in the pharmaceutical industry to perform a variety of unit operations where product contamination is a primary concern. The vessel walls and corresponding impeller are lined with a glass coating to prevent corrosion and provide a smooth surface for superior cleanability [6]. In order to minimize turbulence and reduce shear stress on the product, this style reactor is typically fitted with a retreat-style impeller with low impeller clearance and smoothed edges [9]. As the impeller agitation speed increases, the effects of vortex formation become more apparent and baffling is utilized to decrease liquid surface deformation and maintain mixing efficiency [7]. Common baffling configurations include a fully baffled system of four vertical plates placed evenly throughout the vessel, and a semi-baffled system consisting of a single, beavertail-style baffle.

In this study, CFD is utilized to simulate the power dissipation of a scaled-down model of a glass-lined pharmaceutical reactor equipped with a three-blade RCI. The glass lining has improved resistance to corrosion and has a smooth surface that is easy to clean. The retreat-style impeller is selected to provide improved radial flow while maintaining a relatively low power number with a high Reynolds number. The impeller is placed close to the vessel's bottom such that the system can accommodate a wide range of liquid levels while maintaining mixing efficiency. The smoothed surface on the impeller is also designed to subdue turbulence [6].

As impeller speed increases in the system, the mixing action inside the vessel begins to create a large, centralized vortex and results in systemic mixing inefficiency. Therefore, baffling is often required to prevent significant vortex formation and support mixing effectiveness [7]. The system is modeled using three separate baffling systems, including fully baffled, semi-baffled, and un-baffled. Due to the glass lining, the fully baffled system consists of four vertical plates that are inserted into the vessel and do not come into direct contact with the wall. This setup ensures that vortex formation is kept to a minimum. For the purposes of modeling this type of system using CFD, surface deformation is assumed to be minimal and is effectively ignored in the calculation of power dissipation.

The semi-baffled system includes a single beavertail baffle which helps to eliminate vortex formation while reducing shear [7]. The single beavertail baffle helps to minimize a large amount of surface deformation. In this case, however, the Multiple Reference Frame (MRF) technique is not enough to accurately simulate the system. A time dependent study with the sliding mesh technique is required in order obtain more reasonable results, but at the expense of significantly increased computational time that is highly sensitive to model design. In the un-baffled system, large vortex formation will become an issue with mixing; however, CFD simulation of the Newton number is relatively accurate [12]. A fixed rotor approach is utilized, where the impeller is kept in place and the vessel walls are allowed to rotate in order to simulate the fluid flow. Using this approach, it is expected that mesh construction and modeling assumptions will have a significant impact on results, even for power dissipation studies. Therefore, numbers presented in this study for the un-baffled system using the frozen rotor approach do not

reveal a Newton number independent of the Reynolds number consistent with results achieved in previously conducted experiments.

1.2 Objectives

CFD is utilized to capture the impeller power dissipation for a pharmaceutical reactor using several different system setups, including various impeller speeds, impeller clearances, and baffling configurations. The vessel is modeled after a scaled-down version of a ~61 L De Dietrich reactor, cylindrical in shape with a dished, torispherical bottom. The impeller is modeled after a glassed steel 3-blade retreat impeller, placed vertically and centered inside the vessel. Baffling configurations include fully baffled from four vertical plates with almost zero wall clearance, semi-baffled with a single beavertail style baffle, and un-baffled configuration. Impeller speeds are considered from 20 to 200 RPM. Impeller clearance is considered at separate heights: 40 mm, 100 mm, and 200 mm. The majority of all modeled systems utilize a frozen rotor approach, although a time dependent study is constructed for the semi-baffled system with H/T = 1.0 and impeller clearance at 40 mm. Modelling approach and meshing techniques are presented along with computational assumptions. Comparison between simulated and experimental results is investigated.

CHAPTER 2

THEORETICAL BACKGROUND

2.1 Introduction to Computation Fluid Dynamics

Computational Fluid Dynamics (CFD) is a computational tool that employs numerical methods and algorithms to discretize and solve partial differential equations (PDEs) into solvable systems of equations for the purposes of analyzing fluid flow problems. Partial derivatives from the PDEs are replaced with finite difference quotients, which in turn are utilized to formulate difference equations. The difference equations are algebraic representations of the PDE and are solvable. In CFD, the object or system that is being studied is broken down into a finite number of cells. These cells are arranged throughout the geometry of the system and are commonly referred to as the mesh or the grid [1].

The difference quotients are replaced in the governing flow equations, creating systems of equations with dependent variables at each grid point within the mesh and a computer is used to solve the system. Numerical solutions of the equations are influenced mainly by two types of errors. The first type is discretization error, which is the difference between the exact solution of the PDE and the corresponding solution of the difference equation. This error is usually the cause of systems that fail to converge due to poorly defined boundary conditions. The second type is referred to as round-off error and is caused by calculations errors that originate from the solving computer [1].

2.2 Navier-Stokes and Development of the Governing Equations

Fluid flow is fundamentally governed by three principles: conservation of energy, conservation of mass, and Newton's second law of motion [1]. The corresponding

equations of these principles serve as the basis for the mathematical modeling of fluid motion. For the system being modeling in this work, an assumption is made that the system is isothermal and that the effects of temperature on flow are negligible. Therefore, the energy equation is not considered. For the conservation of mass, consider the continuity equation in conservation form:

$$\frac{\partial \rho}{\partial t} + \nabla \cdot (\rho \mathbf{u}) = 0 \tag{2.1}$$

where ρ is the fluid density, t is time, and $\mathbf{u}$ is the vector field for the velocity of fluid flow [1].

Newton's second law of motion is expressed as the momentum equation as follows:

$$\mathbf{F} = m\mathbf{a} \tag{2.2}$$

where $\mathbf{F}$ is force, m is mass, and $\mathbf{a}$ is acceleration. Sources for this force can be divided into two categories: body forces, such as gravity, and surface forces [1]. Surface forces have two subcategories: pressure distribution and shear/normal stress distributions (i.e., friction). Furthermore, the assumption is made that surface forces are proportional to the velocity gradients (i.e., Newtonian fluid). The momentum equation written out in x, y, and z component form are collectively referred to as the Navier-Stokes equations:

$$\frac{\partial (\rho u)}{\partial t} + \nabla \cdot (\rho u \mathbf{u}) = -\frac{\partial p}{\partial x} + \frac{\partial \tau_{xx}}{\partial x} + \frac{\partial \tau_{yx}}{\partial y} + \frac{\partial \tau_{zx}}{\partial z} + \rho f_x \tag{2.3a}$$

$$\frac{\partial (\rho v)}{\partial t} + \nabla \cdot (\rho v \mathbf{u}) = -\frac{\partial p}{\partial y} + \frac{\partial \tau_{xy}}{\partial x} + \frac{\partial \tau_{yy}}{\partial y} + \frac{\partial \tau_{zy}}{\partial z} + \rho f_y \tag{2.3b}$$

$$\frac{\partial (\rho u)}{\partial t} + \nabla \cdot (\rho w \mathbf{u}) = -\frac{\partial p}{\partial z} + \frac{\partial \tau_{xz}}{\partial x} + \frac{\partial \tau_{yz}}{\partial y} + \frac{\partial \tau_{zz}}{\partial z} + \rho f_z \tag{2.3c}$$

where τ represents the viscous surface forces (normal and shear), f represents the body forces, and **u** is the flow velocity [1].

2.3 Two-equation Turbulence Model: *k*-ε

In the system of interest for this study, the model was expected to operate under turbulent conditions. In order to determine whether the flow can be characterized as laminar, turbulent, or in transition, the ratio of inertial and viscous forces is calculated for each scenario as follows:

$$\text{Inertial force} \equiv (\mathrm{N}D_i)^2 \rho D_i^2 \tag{2.4a}$$

$$\text{Viscous force} \equiv \frac{\mu(ND_i)D_i^2}{D_i} \tag{2.4b}$$

where N is the impeller speed, D_i is the impeller diameter , and μ is the fluid viscosity. After reduction, the ratio of these two forces simplifies to the Reynolds number (dimensionless) [15]:

$$Re = \frac{N_i {D_i}^2 \rho}{\mu} \tag{2.5}$$

In a mixing tank, transition from laminar to turbulent flow usually occurs between Re = 50 and Re = 5000, and can be largely dependent on the power number of the impeller. In a fully baffled system, flow is considered fully turbulent where $\mathrm{Re} > 10^4$. However, in an un-baffled system, flows will not necessary reach full turbulence until approximately $\mathrm{Re} > 10^5$ [13] [15].

Incorporating turbulence into the Navier-Stokes equations is accomplished through the use Reynolds-Averaged Navier-Stokes equations, or RANS [7], which are added on top of Equations 2.3a, 2.3b, and 2.3c. Recall that the governing equations are

computed for each node within the geometry that comprises the system. By considering only the mean flow across each node, the amount of computation is reduced which can aid in helping the system to reach convergence faster [1]. The momentum flux after considering the time-averaged values across each node is referred to as Reynolds stresses. However, this also indicates the significance of the system mesh, that areas where eddies and large turbulence occur should have as dense or fine a mesh as possible to accurately describe the fluid flow in those areas. Several methods have been devised in order to accomplish this and explored later in Chapter 3.

In order to solve for the RANS equations, the assumption is made that the Reynolds stresses are proportional to the averaged velocity gradients, also known as the Boussinesq Hypothesis [7]. This relationship can be illustrated as follows:

$$\rho\overline{\mathrm{u'}_i\mathrm{u'}_j} = \frac{2}{3}\rho k\delta_{ij} + \left[\mu_t\left(\frac{\partial \mathbf{u}_i}{\partial x_j} + \frac{\partial \mathbf{u}_j}{\partial x_i}\right)\right] \tag{2.6}$$

where $\overline{\mathrm{u'}_i\mathrm{u'}_j}$ are the Reynolds stresses and μ_t is the turbulent viscosity [12].

To solve for the Reynolds stresses, a commonly used turbulence model for stirred reactors is the *k*-ε model, where *k* is the turbulence kinetic energy and ε is the rate of dissipation of turbulence kinetic energy [16]. These transport equations are presented as follows:

$$\frac{\partial(\rho k)}{\partial t} + \frac{\partial}{\partial x_i}(\rho \mathbf{u}_i \mathrm{k}) = \frac{\partial}{\partial x_i}\left(\mu + \frac{\mu_t}{\sigma_k}\right)\frac{\partial k}{\partial x_i} + \mathrm{G}_k - \rho\epsilon \tag{2.7}$$

$$\frac{\partial(\rho \varepsilon)}{\partial t} + \frac{\partial}{\partial x_i}(\rho \mathbf{u}_i \varepsilon) = \frac{\partial}{\partial x_i}\left(\mu + \frac{\mu_t}{\sigma_\varepsilon}\right)\frac{\partial \varepsilon}{\partial x_i} + \mathrm{C}_1\frac{\varepsilon}{k}\mathrm{G}_k + \mathrm{C}_2\rho\frac{\varepsilon^2}{k} \tag{2.8}$$

where μ is the dynamic fluid viscosity, μ_t is the eddy viscosity, G_k is the term for turbulence generation [12]. By introducing these additional equations into the model,

additional boundary conditions must also be applied and are derived experimentally. C_1, C_2, σ_ε, and σ_k are those empirical constants: they are listed as follows as they are applied within the CFD model:

$$C_1 = 1.44,\ C_2 = 1.92,\ \sigma_K = 1.00, \sigma_\varepsilon = 1.30 \tag{2.9}$$

The generation of turbulence is dependent on the turbulent viscosity, and defined as follows:

$$G_k = \mu_t \left(\frac{\partial \mathbf{u}_i}{\partial x_j} + \frac{\partial \mathbf{u}_j}{\partial x_j} \right) \frac{\partial \mathbf{u}_j}{\partial x_i} \tag{2.10}$$

where turbulent viscosity μ_t comes from a derivation of k and ε as follows:

$$\mu_t = \rho C_\mu \frac{k^2}{\varepsilon} \tag{2.11}$$

where C_μ is yet another constant determined experimentally and utilized within the model having a value of 0.09 [12]. This relation is commonly referred to as the Kolmogorov-Prandtl Eddy Viscosity Expression. To summarize, the model is employed to solve for k and ε, which in turn are used to find the turbulent viscosity. Using the Boussinesq hypothsis, the RANS equations are computed and applied to the governing equations [12]. Additional body forces are considered later in Chapter 3.

CHAPTER 3

CFD MODELING OF THE PHARMACEUTICAL MIXING SYSTEM INVESTIGATED IN THIS WORK

3.1 Mixing Apparatus

The mixing system studied in this work is a scaled down cylindrical vessel with a torishperical bottom. The actual mixer used previously in experiments carried out by this group was commissioned and paid for by Eli Lilly; fabrication and design was completed with the assistance of Dr. David Brown from the BHR Group (UK) [2]. The tank is comprised of a of a 0.5 mm fluorinated ethylene propylene co-polymer (FEP) rigid film with a refractive index of 1.338. The results of the experimental study using the actual system performed by Banerjee serve as the benchmark comparison for the CFD output as well as other similar studies using a similar setup [2].

In order to correctly model the system under study, the geometry of the tank was measured using a Stanley PowerLock Tape Rule (16 feet), Model 33-116. The internal diameter of the tank is 445 mm. The overall height is 533.4 mm, consisting of a cylindrical height of 431.8 from the top down to the point where the wall begins curvature for the dished bottom, then 101.6 mm to the lowermost point of the dished bottom. At the top of the vessel is a plastic lip that goes around the perimeter that is 12 mm thick and 39 mm wide.

The tank is without a lid and was left uncovered to open air during previous experimentation. The walls and points of curvature of the tank are smooth, uniform, and symmetrical. This is a minor indentation noticeable where the torishperical bottom was molded into the cylindrical top, but is does not appear a significant compromise to the

integrity of the design. There are no points of attachment for baffling, consistent with the glass-lined scaled up version. The assumption is made that the walls remain rigid during the mixing process and that any experimental limitation of data collection do not impart a significant contribution to the results utilized for the comparative study.

3.2 Agitation System

Impeller and baffling geometries were measured used a Neiko Digital Caliper (6 inches with metric LCD display), Model FR-8ZT5-LLNT. The measuring device was calibrated using a Standard Gauge micrometer setting standard (2 inch), Part Number 02164102 with +/- 0.00008 inch precision. The overall length of both the impeller and baffles were measured using an Alvin Flexible Rule (18 inch), Model R590. The impeller is a scaled-down version of a De Dietrich style glassed steel 3-Blade Retreat impeller that is typically used in association with glass-lined vessels [6]. The edges are purposely smoothed to prevent the break-down of the glass coating at high stress, although the scaled-down version is without coating and is exhibiting minor corrosive properties on the blades.

Due to small variations in the geometry for each blade, the measurements were taken for each of the blades and averaged to obtain the final measurement. The radius of the entire impeller is 101.29 mm. Blade thickness is recorded as 12.7 mm and the blade height is 25.4 mm. The blades are angled upwards with a 15° rise, measured using a Westcott protractor (6 inch), Model number 11200. The blades are connected to a cylindrical connecting shaft with a diameter of 25.5 mm and height of 31.9 mm. The main shaft that would connect to the motor and connecting shaft is cylindrical with a 12.7 mm diameter and 470 mm in height.

Special attention and detail is given to the measurement and geometrical construction of the impeller, as this is vital to achieving accurate results in the computational model. The impeller blades are curved in a counter-clockwise position. In order to determine the radius of curvature, the length *a* and height *h* of the inner curve was measured as 89.5 mm and 11.66 mm, respectively. The corresponding radius *r* that describes the curvature was then calculated at 91.7 mm using the trial and error method in conjunction with the following equation:

$$h = r - \sqrt{r^2 - \frac{a^2}{4}} \tag{3.1}$$

The radius of curvature was then utilized to compute the central angle α (62.2°) of the impeller bade, which is necessary in order to generate the curve [3]:

$$\alpha = 2 \arcsin \frac{a}{2r} \tag{3.2}$$

The blades are flush against the connecting shaft and anchored with a recessed screw on the top of the connecting shaft. The screws show signs of rusting, but do not compromise the integrity of the geometry. One additional screw is placed on the side of the connecting shaft to anchor it to the main shaft. The screw slightly protrudes but not significantly enough to enter the model geometry. The tips of each blade are significantly rounded and the edges are smooth. The main shaft protrudes slight out of the bottom of the connecting shaft by 3.08 mm.

The impeller is located centrally within the tank in an upright perpendicular position. Unless otherwise indicated, all computational studies were conducted with an impeller clearance of 40 mm (measured from the impeller bottom to the bottom of the tank). In another scenario, the impeller clearance is increased to 100 mm and 200 mm in

order to detect if power dissipation and the velocity flow fields are affected by impeller vertical clearance. The geometry details of the impeller are presented in Figures 3.1 and 3.2 below.

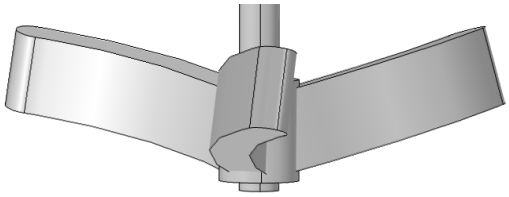

Figure 3.1 Three blade impeller geometry, side view.

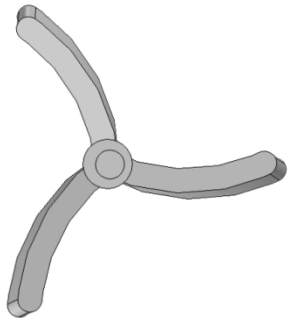

Figure 3.2 Three blade impeller geometry, top view.

3.3 Baffling Setup

Three modelling systems are considered in this work: fully baffled, semi-baffled and un-baffled. In all scenarios, the baffling clearance for the fully-baffled system and semi-baffled system is 101.6 mm (point of curvature in the vessel walls). For the fully baffled system, four vertical plates are inserted into the tank. The plates have a width of 45 mm and are placed symmetrically, against the vessel wall. The plates are evenly spaced between one another and oriented such that the wide part is perpendicular to the rotational flow. The thickness of the plates are not considered and modelled as two dimensional objects. Geometry details of the fully baffled system are presented in Figure 3.3.

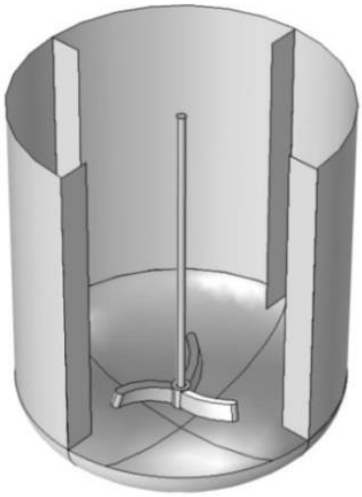

Figure 3.3 Geometry of the fully baffled system, angular view.

The semi-baffled system consists of a single beavertail style baffle. The baffle is placed midway between the impeller main shaft and the vessel wall with 101.6 mm clearance. Measurements are taken using the same caliper and ruler for the impeller. The overall length of the baffle is 445.1 mm and can be divided into three sections: lower, middle, and top. The lower section is cylindrical in shape, 67.7 mm in length with a diameter of 40.12 mm. The middle section is flattened to a thickness of 27.6 mm, where the diameter is 44.6 mm and the length is 152.4 mm. The top section is cylindrical with a length of 225 mm and a diameter of 30.5 mm. As the top section approaches the middle section, it becomes conical in shape, where the cone is 46 mm long and the bottom cone diameter is the same as that of the middle section. Figures 3.4 and 3.5 present the geometry details of the semi-baffled system.

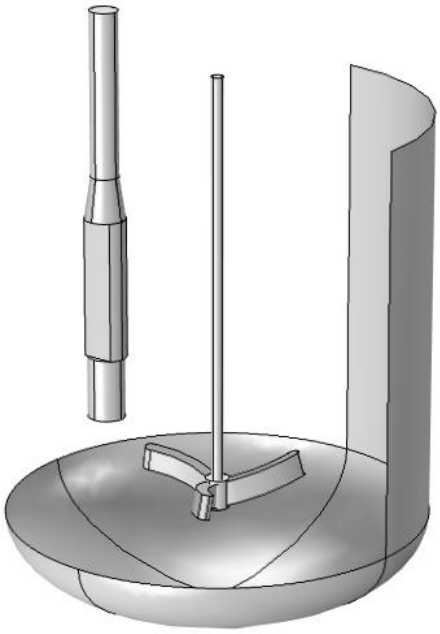

Figure 3.4 Geometry of the semi-baffled system, angular view.

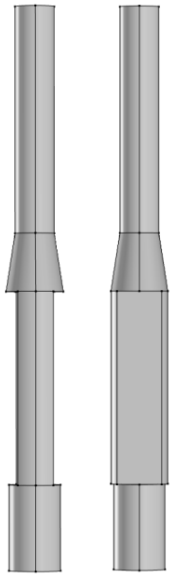

Figure 3.5 Geometry study of the beavertail style baffle.

3.4 Unstructured Adaptive Grid Technique Used in This Work

The meshing utilized on the system takes into consideration two simplifying assumptions. First, the assumption is made that the system is isotropic as defined through the *k*-ε modelling approach (i.e., the Reynolds stresses are proportional to the rate of deformation in all directions) [7]. Second, the assumption is made that the fluid is incompressible at all times within the system throughout the mixing process.

Additionally, the mesh was refined as much as possible while keeping the computation time to a minimum. In a preliminary study using the fully baffled system, the meshing was adjusted to test how power dissipation is affected as the number of nodes is changed. Based on this information and the time of convergence, the mesh was

selected to contain 472,258 node for the fully-baffled system, then 356,211 and 178,443 nodes for the semi-baffled and un-baffled systems, respectively.

The system mesh is an unstructured, free tetrahedral geometry. The maximum and minimum elemental sizes of the nodes are 34.5 mm and 7.2 mm, respectively. Although this seems rather course for a vessel having a diameter of 445 mm, this is not uniform across the entire geometry. Since the primary goal of this study is to determine systemic variations, the mesh is adaptive to selectively chosen boundaries and edges. In other words, the node size becomes finer as it approaches areas where turbulence is more likely to occur, including the surfaces of the impeller, rotating shaft, and baffling. For these structures, the node size range is considerably smaller, with the maximum and minimum sizes of 10.6 mm and 0.7 mm, respectively.

The intricate geometry of the vessel ensures that the element growth rate remains very low and node sizes tend to stay closer to the minimum size. See Figures 3.6, 3.7, 3.8, and 3.9 for visual depictions of how the meshing is applied. Note that a cylinder can be seen in the second figure. This is the rotating domain that will be utilized in the bulk of the computation experimentation using a multiple reference frame technique and will be explained in the following sections.

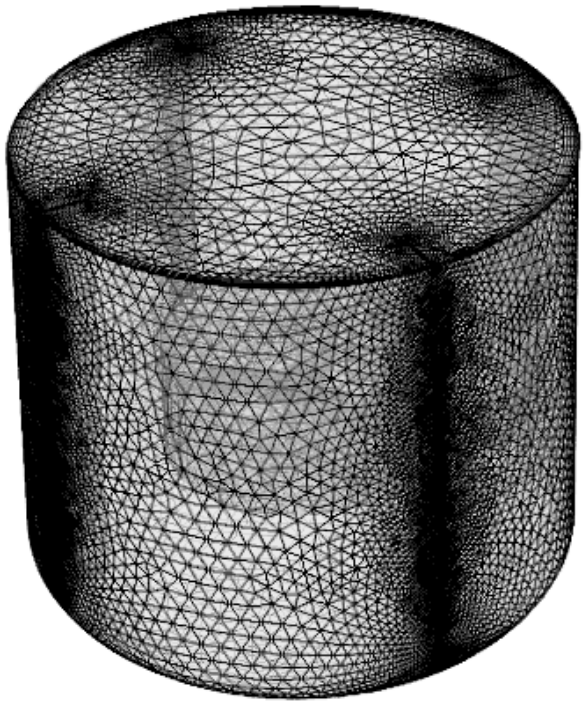

Figure 3.6 Meshing of fully baffled system with angled view.

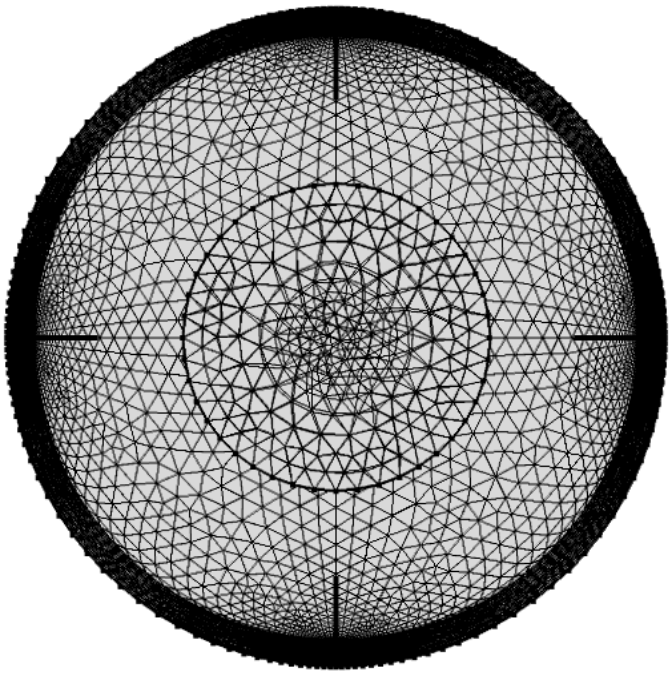

Figure 3.7 Top view of meshing for the fully baffled system.

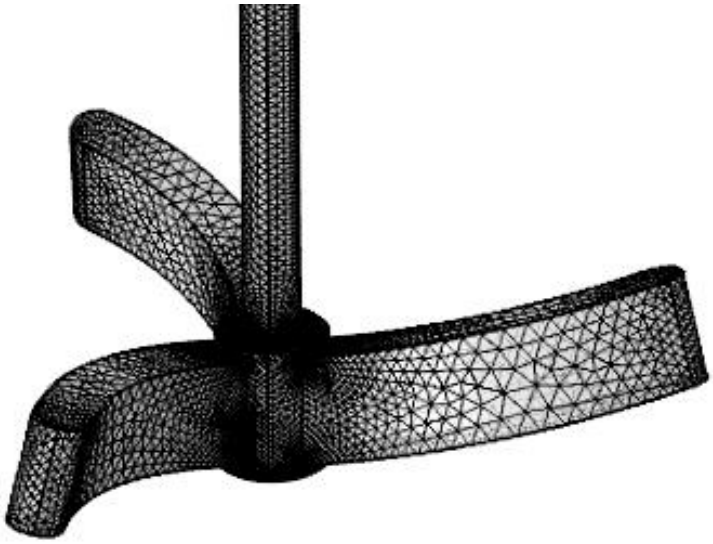

Figure 3.8 Retreat blade impeller meshing with free tetrahedral technique.

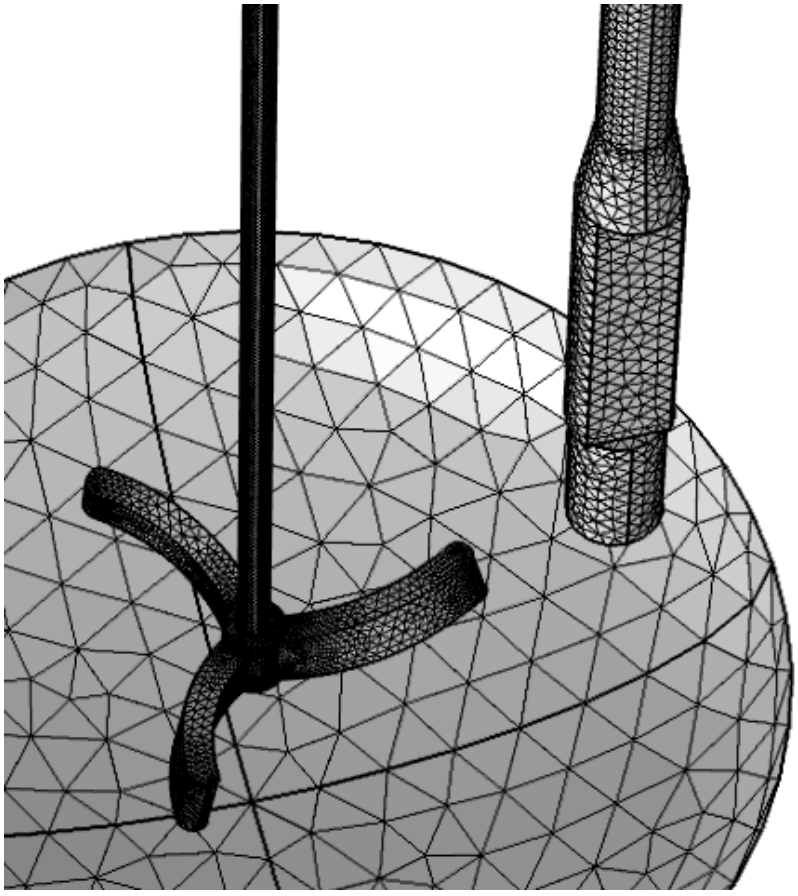

Figure 3.9 Angular view of semi-baffled system with various meshing refinement.

Figures 3.6 and 3.7 depict the meshing for the fully baffled system. Note that the nodes become smaller as they approach the baffling as well as the rotating impeller shaft. Figures 3.8 and 3.9 show the grid for the semi-baffled system using a single beavertail baffle. Figure 3.9 specifically shows an angular view of the impeller, baffle, and dish bottom of the vessel with the walls removed. Note the scaling of mesh generation, which becomes more refined in areas where it has greater influence on the flow fields.

3.5 Computational Approaches Used in This Work

A variety of computational approaches were implemented in the CFD code of this work to model hydrodynamically the mixing system studied here, including the single reference frame (SRF) model, the multiple reference frame (MRF) model, and the sliding mesh (SM) model.

3.5.1 Multiple Reference Frame Approach

In each baffled system, the fluid flow is in reality unsteady and therefore time dependent. However, an alternative method is utilized that significantly reduces computation and is capable of producing accurate steady state approximations of global numbers such as the power dissipation and Newton number [9]. The assumptions are made that the rotational speed is constant and that impeller-baffle interaction is insignificant in the global system. Using the Multiple Reference Frame (MRF) approach, the volume within the vessel is divided into two reference frames or domains: the rotating domain and the stationary domain.

A boundary is created that encapsulates the impeller section: inside this area is the rotating domain and contains the rotating machinery. Within this area, the impeller does

not move as defined by the model; rather, flow is considered around the impeller geometry, where centrifugal and Coriolis forces are added to the governing equations 2.3a, 2.3b, and 2.3c in order to account for the rotational effect [5]:

$$\mathbf{F} = \mathbf{F}_{\text{Coriolis}} + \mathbf{F}_{\text{Centrifugal}} = -[2m\Omega \times \mathbf{v}_r + m\Omega \times (\Omega \times \mathbf{r})] \quad (3.3)$$

where Ω is the angular velocity vector, v is velocity and *m* is mass.

This approach considers the instantaneous flow fields at the fully developed stage of impeller speed, and thereby provides a means to produce a steady state approximation without changing the mesh positioning. Outside this boundary is the stationary domain that contains the non-rotational components, including baffling and walls. Flow continuity is applied at the interface of these two regions for vector quantities of velocity and the velocity gradients [5].

The fully baffled system utilizes the MRF approach; see Figure 3.10 for a side view of the geometry.

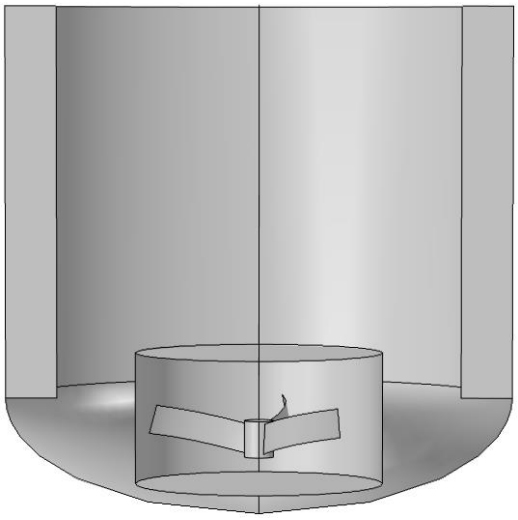

Figure 3.10 Side view of the geometry, Multiple Reference Frame, fully baffled system.

3.5.2 Single Reference Frame Approach

In the un-baffled system, only one rotating reference frame is utilized in the simulation, herein referred to as the Single Reference Frame (SRF). In this case, the impeller is held in a fixed position and the outside vessel wall is allowed to rotate. As in MRF, fluid flow is considered around the impeller geometry and centrifugal and Coriolis forces are applied in each scenario.

3.5.3 Sliding Mesh Approach and Free Surface Deformation

The semi-baffled system is truly a time dependent model and is also influenced by surface degradation due to vortex formation. Therefore, a steady state approximation is not appropriate and may not accurately describe the system under turbulent conditions. In the sliding mesh approach, the grid within the rotating domain is physically rotated about the impeller and moved is small, discrete steps in order to better simulate flow. The system is then solved for at each step in an iterative process until convergence is reached [1]. The system is simulated until the torque measurements on the impeller reach a quasi-steady state:

$$\frac{\Delta M}{\Delta t} = 0 \tag{3.4}$$

In this case, the interface with the stationary domain will not line up perfectly and an interpolation step is needed in order to model the corresponding velocity gradients into the stationary domain [12].

A few additional steps are required for system setup. The main impeller shaft is removed in order to accommodate the free surface concept presented earlier. The impact to results from this minor alteration is considered insignificant. The rotating domain is modeled so that only the impeller section is encapsulated within the stationary domain

[14]. Figures 3.11 and 3.12 demonstrate the geometries used in the Sliding Mesh approach. The surface area of the stationary domain that is exposed to the air is assumed to have normal atmospheric pressure (p = 101325 Pa).

It is desired to model the vortex formation in the un-baffled system. In these scenarios, viscous stress τ_s is modelled at the surface as follows:

$$\tau_s \cdot \mathbf{n}_i = -\mathrm{P}\mathbf{n}_i + \mathrm{F}_s = -\mathrm{p}\mathbf{n}_i + \sigma\{(\nabla_s \cdot \mathbf{n}_i)\mathbf{n}_i - \nabla_s\} \quad (3.5)$$

where $\mathbf{n}_i$ is the normal, P is the outside pressure, F_s is the surface tension force, σ is the surface tension coefficient, and ∇_s is the surface gradient [5]. Consider the definition of the Contact Line to be the point where the liquid, air, and vessel wall meet together. At this intersection, a slip boundary condition is applied that allows that Contact Line to move free freely along the vessel wall. For simplicity, the contact angle is held constant at 90°.

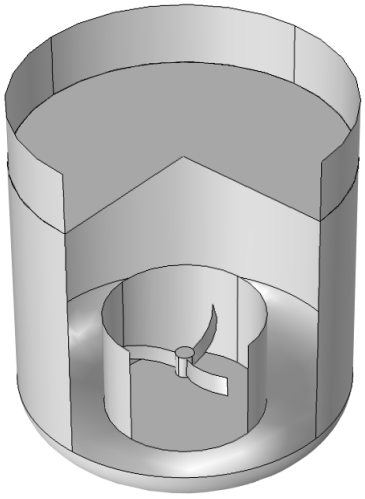

Figure 3.11 Sliding Mesh geometry with submerged rotating domain, un-baffled.

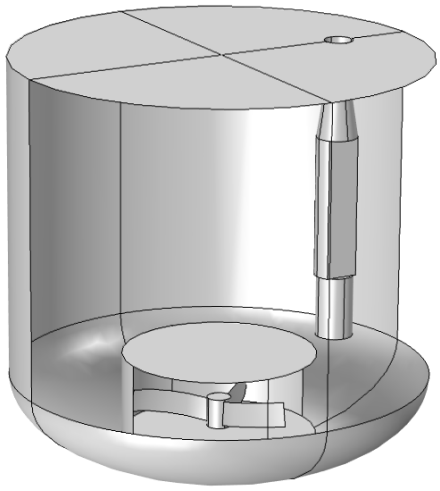

Figure 3.12 Sliding Mesh geometry with submerged rotating domain, semi-baffled.

There are a few drawbacks to this technique. Recall that the mesh within the rotating domain does not deform; therefore, the effects of vortex formation on the power requirements of the impeller may not be fully realized. Furthermore, the simulated surface deformation can never go past the rotating domain and the system may not converge. For these reasons and the complexity of model setup, the free surface is only considered for the purposes of simulating the vortex.

3.6 Liquid Free Surface Modeling

In fully baffled mixing systems, the liquid free surface is nearly perfectly horizontal because of the presence of the baffles that convert some of the tangential flow generated by the impeller into axial flow. The liquid free surface is similarly horizontal in partially baffled systems, although a very small asymmetric vortex can be observed. Therefore, in this work, the liquid free surface for fully baffled and partially baffled systems was always assumed to be flat.

However, in the unbaffled system, liquid free surface may actually inflect and create a vortex depending on the agitation intensity. In such a case, the liquid exhibits a tangential motion from the rotating impeller that, as the impeller speed increases, begins to approximate a solid body rotation and mixing efficiency deceases. Furthermore, the quasi-rigid body of fluid produces a rotational inertial force centered on the rotating shaft of the impeller [12]. This corresponds to a dynamic pressure gradient that is lowest in the center, gradually increasing towards the wall of the vessel, producing a central vortex surface deformation. As expected, the free surface of the liquid within the cylindrical vessel assumes a parabolic surface shape from the centrifugal force [5].

As the Reynolds number increases, the vortex will begin to appear without baffling and the Froude number increasingly becomes a factor [15]. The Froude number, Fr, is the ratio of inertial and gravitational forces:

$$\mathrm{Fr} = \frac{DN^2}{g} \tag{3.6}$$

This equation clearly demonstrates that Fr will increase as impeller speed increases.

Vortex formation is undesirable as mixing efficiency is diminished [7]. In physical experiments, evidence of the vortex has been shown to significantly reduce the power dissipation of the system, and therefore may produce faulty CFD results if the forces that induce surface deformation are not considered in the modeling approach [5] [10] [14]. Three methods are generally utilized in order to minimize vortex formation: baffling, offsetting the impeller shaft, and angling the impeller shaft in a non-perpendicular fashion [7].

Centrifugal forces are accounted for within each modelling scenario. However, in order to model vortex formation effectively using CFD, a time dependent study is a requirement. This is very computationally expensive and is only performed on the un-baffled systems in this study. The approach was taken to submerge the reference frame such that it is encapsulated by the spatial frame, where the spatial frame presents the liquid surface [14]. Influence from the impeller shaft is ignored and removed from the geometry. The reference frame surrounds the impeller, whereas the spatial frame comprises the rest of the volume within the vessel.

In the geometry of the sliding mesh technique, there exists an exposed surface of the spatial frame to the air, creating a three-phase intersection: the liquid within the

spatial frame, the vessel wall, and the air to which the surface is exposed. The assumption is made that external conditions such as pressure and temperature within the air have a negligible impact on vortex formation. Although the mesh within the reference frame cannot be altered, the nodes contained within the spatial frame can be deformed to model the surface deformation and takes into consideration the surface tension forces within the rotation system.

3.7 Impeller Power Number Calculation

For each scenario ran on the model, it is desired to obtain the power dissipation. The torque applied to the impeller is calculated by taking the force applied to the impeller blade and integrating across the surface of the impeller. This is multiplied by three to account for each of the blades of the impeller:

$$\mathrm{M} = \ 3 \cdot \int \mathbf{r} \times \mathbf{F} \, dA \tag{3.7}$$

where M is the torque, A is the surface area of the impeller blade, and F is the force applied [7]. The torque from the rotating shaft itself is negligible and ignored for practical purposes. Torque is then multiplied by the angular velocity to obtain the power required to overcome the magnitude of forces that resist impeller rotation at a specified speed. Note that the impeller speed is in Hertz:

$$\mathrm{P} = \Omega \mathrm{M} = 2\pi N_i \mathrm{M} = \ 6\pi N_i \int \mathbf{r} \times \mathbf{F} \, dA \tag{3.8}$$

where P is power [7]. When flow within the vessel is fully turbulent, power is also approximated from the kinetic energy per unit volume of the liquid multiplied by the flow from the impeller. For the volumetric flow rate Q, recall the standard equation:

$$Q = v \cdot A \tag{3.9a}$$

where A is the cross-sectional vector area [10]. However, if the impeller blade width W is considered proportional to the impeller diameter D_i and the impeller speed is considered at the tip of the impeller blade, the following relationship emerges:

$$Q = v \cdot A = \left(2\pi N_i \cdot \frac{D_i}{2}\right)\left(2\pi W \cdot \frac{D_i}{2}\right) = (\gamma \pi N_i \cdot D_i)\,(\pi W D_i) \tag{3.9b}$$

The above equation includes γ as a scalar to accommodate discrepancies in actual versus ideal velocities:

$$Q = \gamma \cdot \pi^2 \cdot N_i \cdot D_i^2 \cdot W \tag{3.9c}$$

The kinetic energy per unit volume $\left(\frac{k}{V}\right)$ follows a similar substitution for velocity:

$$\frac{k}{V} = \frac{\frac{1}{2}mv^2}{V} = \frac{1}{2}\frac{m}{V}v^2 = \frac{1}{2}\rho v^2 \tag{3.10a}$$

$$\frac{k}{V} = \frac{1}{2}\rho v^2 \propto \frac{1}{2}\rho\left(\gamma \cdot 2\pi N_i \cdot \frac{D_i}{2}\right)^2 = \frac{1}{2}\rho\gamma^2\pi^2 N_i^2 D_i^2 \tag{3.10b}$$

If W is proportional to D_i, then Equation 3.9c and 3.10b are combined to formulate a final relationship with the power dissipation:

$$P = Q \cdot \frac{k}{V} = (\gamma \cdot \pi^2 \cdot N_i \cdot D_i^2 \cdot W)\left(\frac{1}{2}\rho\gamma^2\pi^2 N_i^2 D_i^2\right) \propto \frac{1}{2}\pi^4\gamma^3\rho N_i^3 D_i^5 \tag{3.11}$$

After the rearranging of terms, the dimensionless Newton number N_p is obtained [7] [10]:

$$N_p = \frac{P}{\rho N_i^3 D_i^5} \tag{3.12}$$

Power and the impeller Newton number will be the primary means of evaluating the CFD modelled systems. In the fully and semi baffled systems, it is expected that N_p will be a function of the Reynolds number in laminar flow [10]. In turbulent flow, however, inertial forces will dominate and the Newton number will become proportional

to $\rho N_i^3 D_i^5$, essentially remaining constant. In the un-baffled system, vortex formation increases with impeller speed and the Froude number becomes part of the equation [15]. Therefore, a decreasing trend in the Newton number is predicted.

An alternative method of calculating the power dissipation is possible but may not be as robust as that presented in Equation 3.8. If the power is considered per unit mass, the result can be equated to the turbulent energy dissipation rate ε:

$$\varepsilon = \frac{\mathrm{P}}{\rho \mathrm{V}}, P = \varepsilon \rho \mathrm{V} \tag{2.19}$$

where P is power and V is the liquid volume within the vessel [12]. For the vessel utilized in this study, liquid volume of the tank is estimated assuming the geometry consists of a cylindrical wall conjoined with a halved ellipsoid:

$$V = \pi r^2 (l - c) + \left(\frac{1}{2}\right)\left(\frac{4}{3}\right)\pi r^2 c \tag{2.20}$$

where r is the tank radius, l is the liquid height inside the tank, and c is the radius of the ellipsoid along the z-axis [3]. From prior measurements, r is 222.5 mm, l is 445 mm, and c is 101.6 mm. The tank volume is calculated as 0.0654 m^3. The fluid properties of the liquid used in the experimental system is assumed to be deionized water and low viscosity [2].

3.8 Summary of the Modeling Procedure Used in This Work

The CFD models are designed to mimic experimental results in order to gauge accuracy of the computational assumptions, techniques, and equations presented in the theoretical section of this paper. Three models are built separately, one for each baffled/un-baffled

system. Computer and software specifications are presented in Appendix B. The basic design process consists of the following steps:

1. Model selection: Three models are considered based on the baffling system selected for simulation. The standard k-ε turbulence model is selected for running all scenarios with RANS. Fluid is considered incompressible; temperature, density, and dynamic viscosity are all held as constants: 293 K, 998.2 kg/m^3, and 993×10^{-6} Pa·s, respectively.
2. Geometry: The vessel, impeller, and baffling system are created according to the specifications outlined in Chapter 3. Careful consideration is given to impeller design and removing edges along smooth surfaces that were created during the design process in order to create uniform meshing.
3. Reference framing: Boundaries are created that divide the geometry into rotating and stationary domains. When the MRF or Sliding Mesh approach is selected, the rotating domain is submerged to encapsulate the impeller only, as displayed in Figures 3.11 and 3.12. Flow continuity is assigned to this boundary, allowing velocity gradient information to flow from the rotating to the stationary domain. At this point, the impeller speed is defined and rotational direction is set to the negative angular velocity. Rotating machinery is distinguished from the interior walls (i.e., baffling). Surface roughness is ignored for simplification of computation. Also for the sliding mesh approach, the stationary domain allows for surface deformation and, consequently, a condition for the mesh (the stationary domain only) to become adaptive to the vortex formation, including a slip condition along the inside

vessel walls. The surface tension coefficient is initially set at 7.28×10^{-2} N/m and the contact angle is held constant at 90°. The fluid above the liquid is defined as normal air with an atmospheric pressure application (101325 Pa).

4. Meshing: The grid is applied using an adaptive, free tetrahedral technique. See Chapter 2 for further details. Finer meshing is applied for the impeller, baffling, and flow continuity between the rotating and stationary domains.
5. Study: The modeling technique will define how the study will proceed. For the MRF approach, the model at this point is ready for computation. For the sliding mesh study, the model is first run using the MRF approach. The results will then serve as the initial solution for the time dependent study in order to minimize computation time. The time dependent study is carried out to cover several rotations under the specified impeller speed. For instance, when impeller speed is 75 revolutions per minute (RPM), or 1.25 Hz (1/s), the system is ran to cover a span of 40 seconds, solving the system in 0.1 second intervals. Literature suggests that a quasi-steady state is reached within 30 revolutions [9].

CHAPTER 4

RESULTS

4.1 Power Numbers for Varying Baffling Systems and Impeller Speeds

Impeller speed in the simulations is varied between 20 RPM and 200 RPM. At each speed the model is ran independently until convergence is reached with a residual error of less than 10^{-6}, which equates the sum of terms in partially converged solutions. The first system considered is the fully baffled system, which is run using the MRF approach. Liquid height is set equal to the vessel diameter and impeller clearance is 40 mm from the torispherical bottom. Time to convergence averages 7.5 hours per scenario.

Calculating the Reynolds number reveals that the flow is turbulent flow for all impeller speeds considered in this system. Furthermore, the expectation is that the inertial forces will dominate and the power will become proportional to $\rho N_i^3 D_i^5$, the denominator of the Newton number N_p [15]. After convergence in the system is reached, the torque is calculated on the surface of the impeller blades and power is calculated using Equation 3.8. Summary of the data for this series of computations is presented in Table 4.1 below.

Table 4.1 Newton Numbers for the Fully Baffled System, H/T = 1

Agitation Rate Ni (RPM)	Reynolds Number Re	Torque M (N·m)	Power P (W)	Newton Number Np
20	1.38E+04	0.00447	0.009	0.743
50	3.44E+04	0.0279	0.146	0.741
75	5.16E+04	0.0630	0.495	0.744
100	6.88E+04	0.111	1.164	0.739
150	1.03E+05	0.250	3.932	0.739
200	1.38E+05	0.444	9.296	0.737

In the fully baffled system, the Newton number remains fairly constant at each impeller speed. Figure 4.1 clearly illustrates that that in turbulent flow, Np becomes independent of Reynolds number, which is consistent with our expectations. There is a very slight decrease in the Newton number as the agitation rate increases; however, it is not statistically significant and is possibly due to residual error in the calculation process. On average, the Newton in turbulent flow remains around 0.74. Figures 4.2, 4.3, and 4.4 depict the normalized velocity flow fields across each grid element.

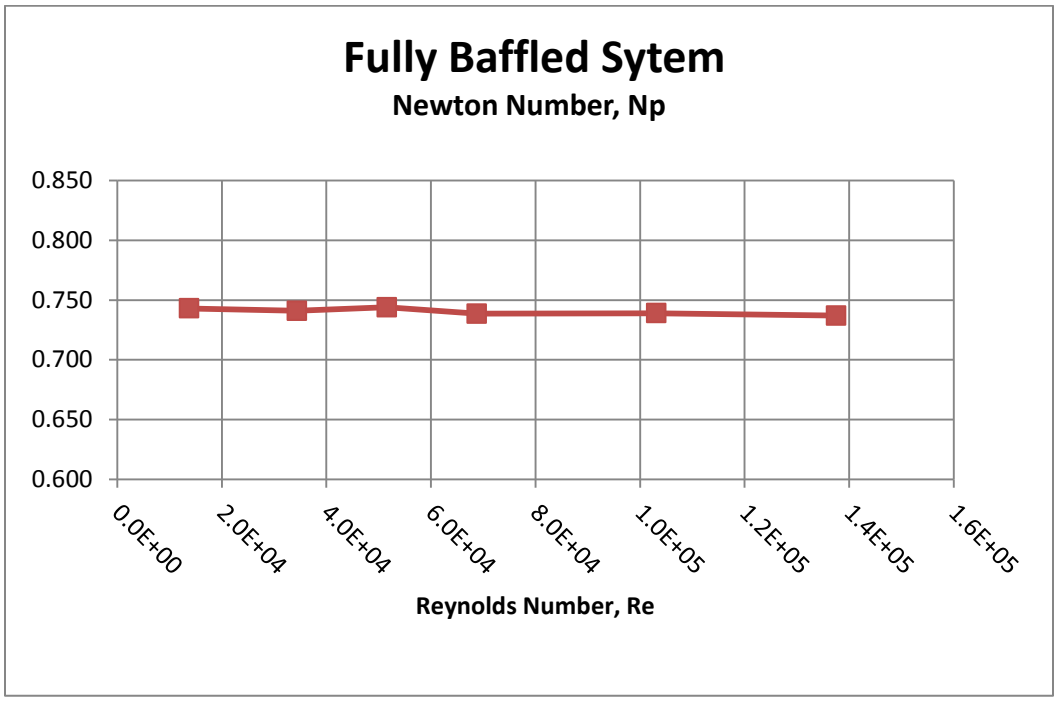

Figure 4.1 Plot of Newton numbers for the Fully Baffled System, H/T = 1.

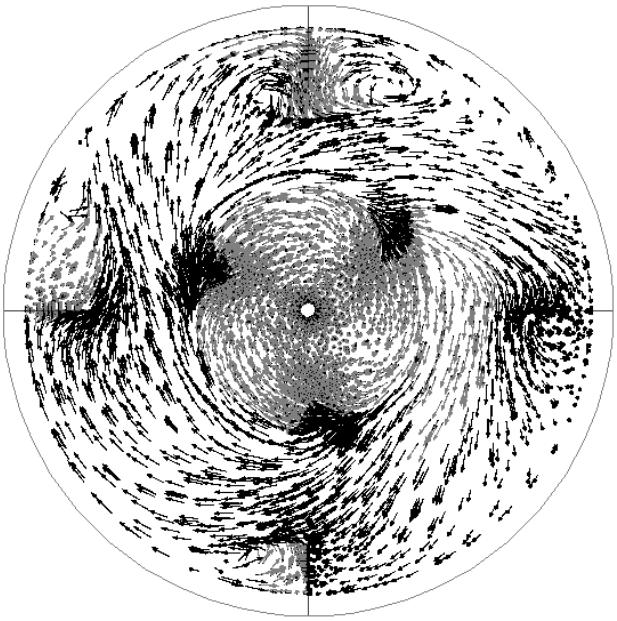

Figure 4.2 Top view of the velocity profile, fully baffled system, 100 RPM, normalized vector flow field across each element, cross sectional slice of the xy-plane 100 mm from the liquid surface.

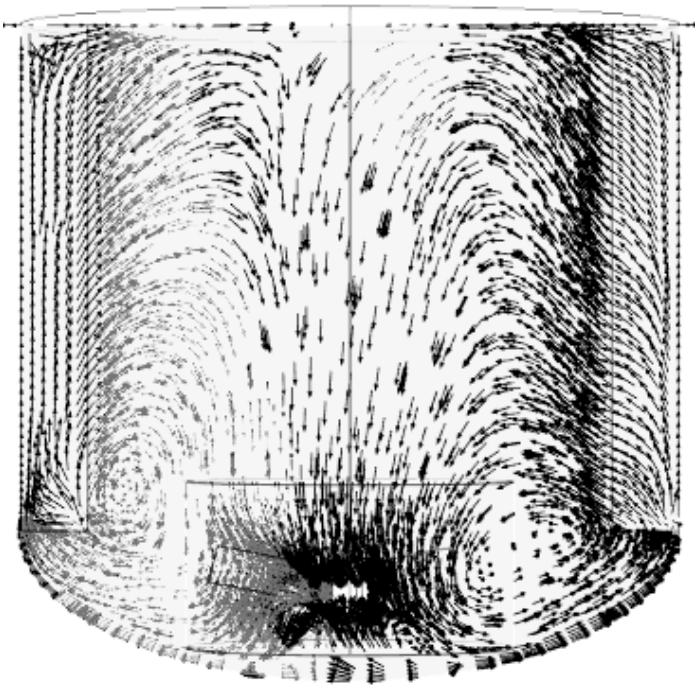

Figure 4.3 Velocity profile of the fully baffled system, side view, 100 RPM, normalized vector flow field across each element, cross sectional slice of the yz plane down the center of the vessel.

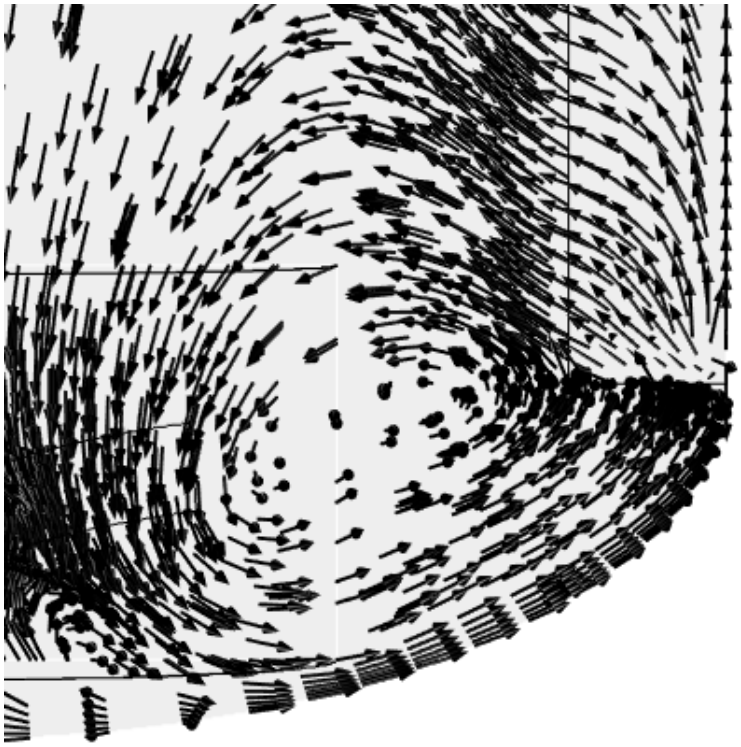

Figure 4.4 Close up of the velocity profile around the impeller, fully baffled system, 100 RPM, normalized vector flow field across each element, cross sectional slice of the yz plane down the center of the vessel.

The next system considered is the semi-baffled system with a single beavertail-style baffle. The same series of impeller speeds are run in the model using the same parameters. For these simulations, impeller clearance was set at 40, H/T = 1, and agitations speed is considered from 20 to 200 RPM. Surface deformation is not in consideration. Results are based on the MRF approach and presented in Table 4.2 below. Time to convergence averages 8.1 hours per scenario.

Table 4.2 Newton Numbers for the Semi-baffled System, H/T = 1

Agitation Rate Ni (RPM)	Reynolds Number Re	Torque M (N·m)	Power P (W)	Newton Number Np
20	1.38E+04	0.00378	0.008	0.627
50	3.44E+04	0.0236	0.124	0.627
75	5.16E+04	0.0532	0.418	0.628
100	6.88E+04	0.0950	0.995	0.631
150	1.03E+05	0.212	3.329	0.626
200	1.38E+05	0.377	7.896	0.626

In this system, there is a considerable decrease the Newton number as a result of the decreased power consumption from the use of a single baffle. Figure 4.5 illustrates that the Newton number remains essentially constant at each impeller speed. Figures 4.6 and 4.7 depict the normalized velocity flow fields across each grid element.

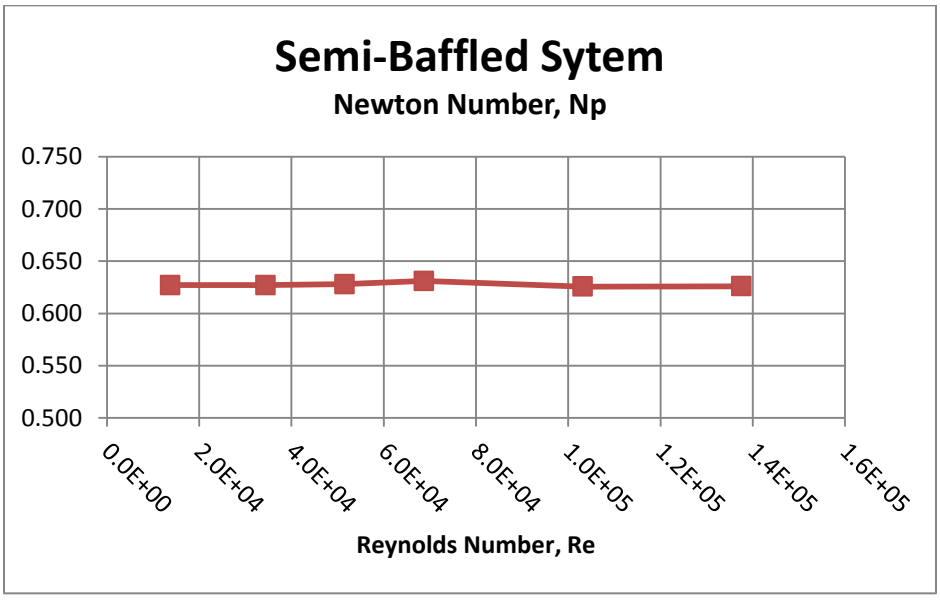

Figure 4.5 Plot of the Newton number in the semi-baffled system, H/T=1.

Figure 4.6 Top view of the velocity profile, semi-baffled system, 100 RPM, normalized vector flow field across each element, cross sectional slice of the xy-plane 100 mm from the liquid surface.

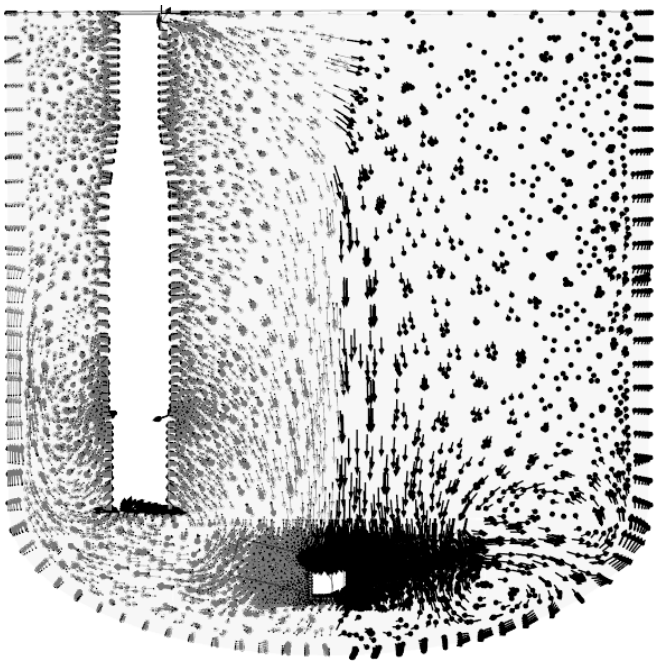

Figure 4.7 Velocity profile of the semi-baffled system, side view, 100 RPM, normalized vector flow field across each element, cross sectional slice of the yz plane down the center of the vessel.

As in indicated in Chapter 3, the semi-baffled system requires a time dependent study in order to accurately describe the fluid flow. Therefore, the results of the scenario above for 100 RPM are utilized as initial conditions for the sliding mesh technique over the course of 40 seconds in 0.1 second intervals. Impeller clearance is 40 mm. Time to convergence was approximately 64 hours. Torque measurements are taken across the impeller blades at each time interval and used to calculate power. After approximately 37 revolutions, a quasi-steady state is reached and power becomes linear over time. Between 45 and 55 revolutions, power essentially becomes 0.826 W with a standard deviation of less than 6.15E-04 W. Using Equation 3.12, the Newton number for the semi-baffled system at 100 RPM (Re = 6.88E04) is 0.523. Details are presented in Figure 4.8 below and the full set of data is given in Appendix C.

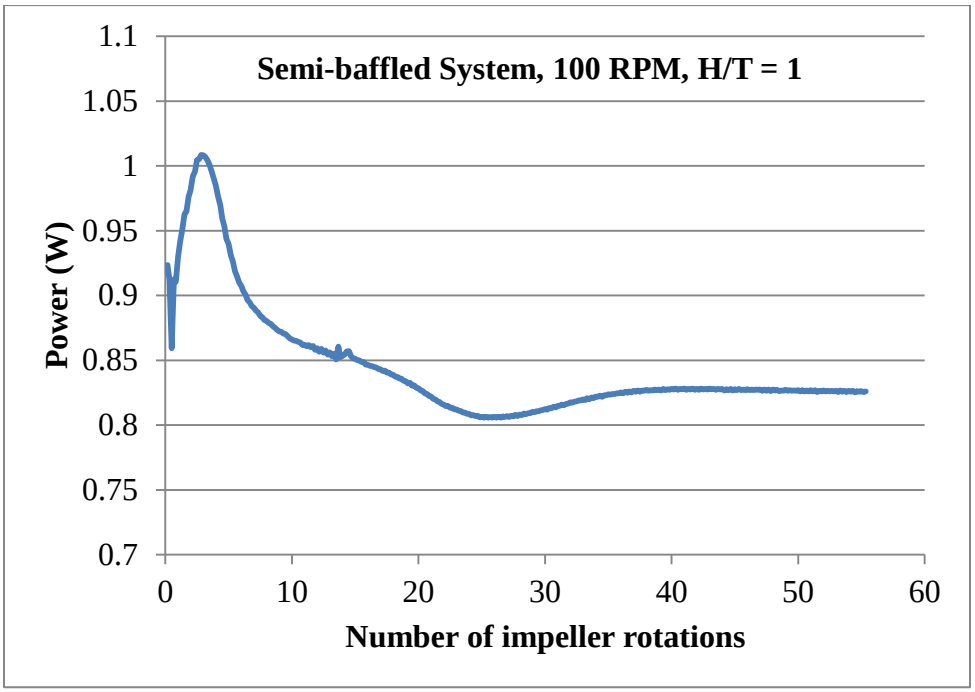

Figure 4.8 Power measurements, semi-baffled time dependent study.

Finally, this series of computations end with the un-baffled system. Again, the same experiments are run using the same parameters as earlier. Impeller clearance set to 40 mm. Time to convergence was approximately 3.5 hours per scenario. Results for the un-baffled system using the SRF approach are presented in Table 4.3 below.

Table 4.3 Newton Numbers for the Un-baffled System, H/T = 1

Agitation Rate Ni (RPM)	Reynolds Number Re	Torque M (N·m)	Power P (W)	Newton Number Np
75	5.16E+04	0.0263	0.207	0.311
100	6.88E+04	0.0471	0.494	0.313
150	1.03E+05	0.105	1.64	0.309
200	1.38E+05	0.187	3.91	0.310

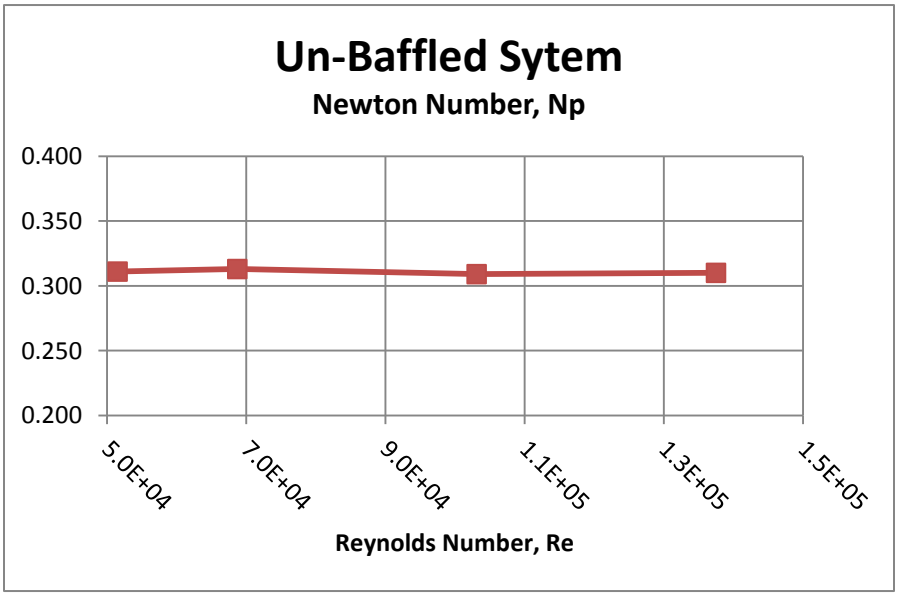

Figure 4.9 Plot of the Newton number in the un-baffled system, H/T=1.

4.2 Power Numbers for Varying Impeller Clearance

The change in impeller clearance is considered for the fully baffled system and semi-baffled systems only. Three separate clearances are studied for the fully baffled system: 40 mm, 100 mm, and 200 mm. Two separate clearances are studied for the semi- baffled system: 40 mm and 100 mm. At 40 mm, the results have already been obtained in Section 4.1 and presented again here for comparative purposes. By increasing impeller clearance, the flow pattern for the entire system may change and the effect on power consumption is unknown. Aside from altering impeller clearance, all system parameters remain the same as the setup in Section 4.1. Data for the impeller clearance is presented in Tables 4.4 and 4.5.

Table 4.4 Newton Numbers, Fully Baffled, H/T = 1, Impeller Clearance = 100mm

Agitation Rate Ni (RPM)	Reynolds Number Re	Torque M (N·m)	Power P (W)	Newton Number Np
20	1.38E+04	0.00456	0.010	0.757
50	3.44E+04	0.0284	0.149	0.755
75	5.16E+04	0.0641	0.503	0.757
100	6.88E+04	0.112	1.176	0.746
150	1.03E+05	0.254	3.996	0.751
200	1.38E+05	0.452	9.473	0.751

Table 4.5 Newton Numbers, Fully Baffled, H/T = 1, Impeller Clearance = 200mm

Agitation Rate Ni (RPM)	Reynolds Number Re	Torque M (N·m)	Power P (W)	Newton Number Np
20	1.38E+04	0.00463	0.010	0.769
50	3.44E+04	0.0291	0.152	0.773
75	5.16E+04	0.0636	0.500	0.751
100	6.88E+04	0.115	1.204	0.764
150	1.03E+05	0.256	4.021	0.756
200	1.38E+05	0.457	9.571	0.759

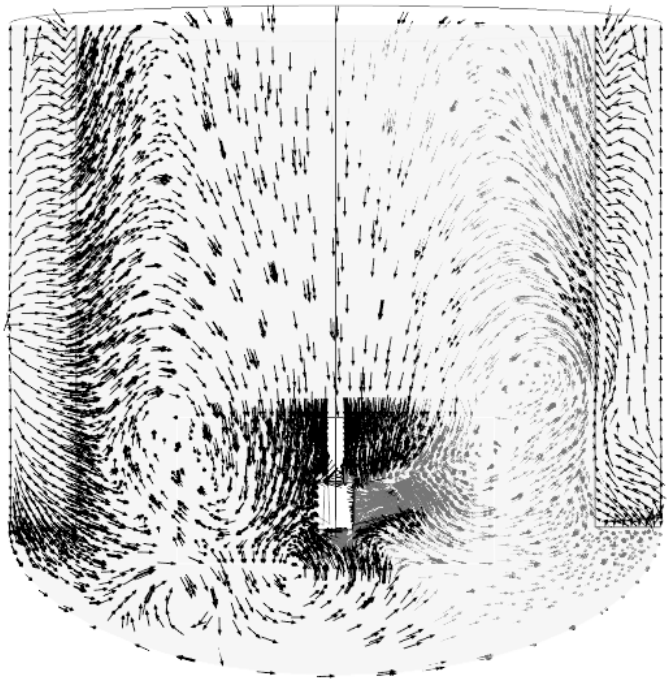

Figure 4.10 Velocity profile of the fully baffled system, side view, 100 mm clearance, 100 RPM, normalized vector flow field across each element, cross sectional slice of the yz plane down the center of the vessel.

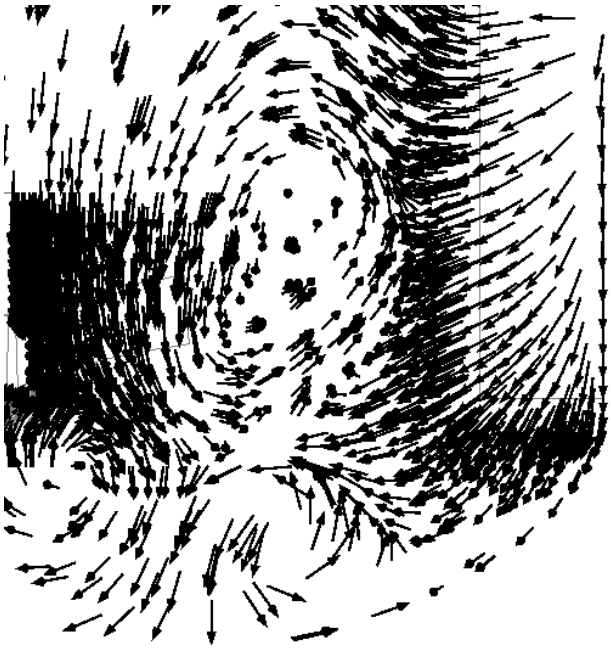

Figure 4.11 Close up of velocity around the impeller, fully baffled, 100 mm clearance, 100 RPM, normalized vector flow field across each element, cross sectional slice of the yz plane down the center of the vessel.

The newton number distribution across multiple rotational speeds when impeller clearance is increased to 200 mm is surprisingly close to the results achieved at 100 mm clearance. The Newton number remains fairly constant in the turbulent environment, averaging approximately 0.76 between 20 and 200 RPM. Figures 4.10 and 4.11 depict the normalized velocity flow fields across each grid element. From the velocity profile, there is considerable interaction between the baffling and flow from the impeller. In contrast to the velocity cross section profile in Figure 4.11, the vortex is more developed, as evidenced in the lower left right quadrant immediately under the plate baffling. Also, the velocity gradients closer to the surface appear more oriented towards the center as opposed to Figure 4.13, where the orientation is more parallel with the impeller main shaft. Finally, the vortex immediately under the impeller is less pronounced. Figure 4.12 shows the similarities in Newton number between the clearances.

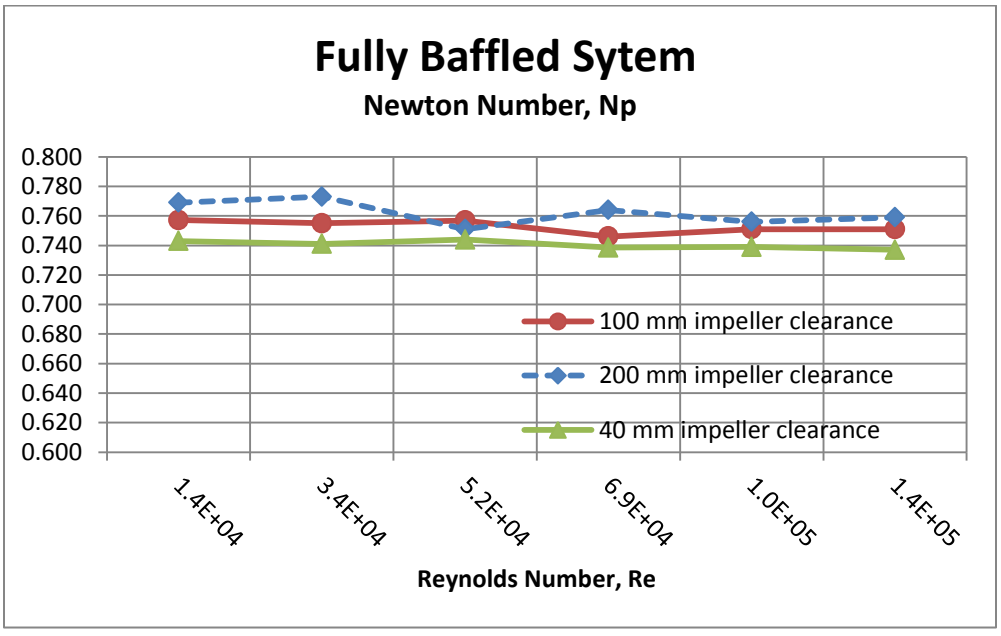

Figure 4.12 Plot of Newton number, fully-baffled system, varying impeller clearance.

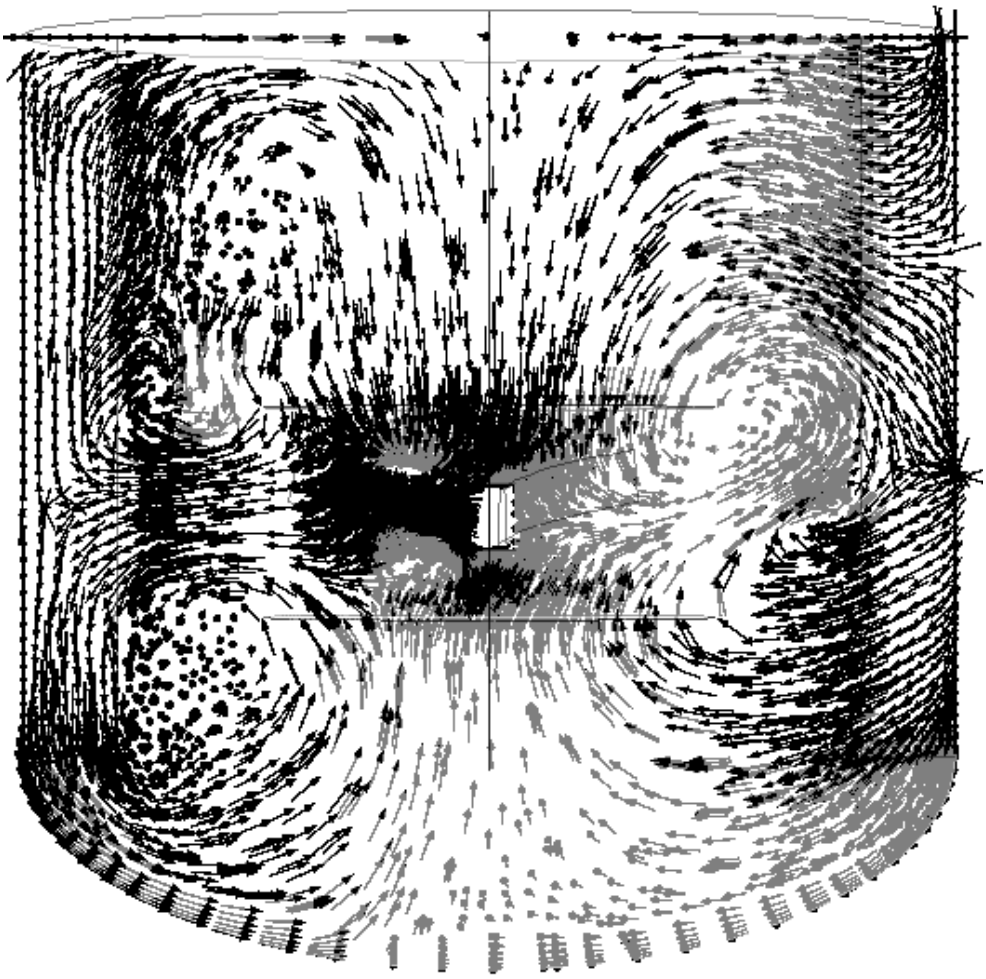

Figure 4.13 Velocity profile, fully baffled system, impeller clearance set to 200 mm, 100 rpm, normalized vector flow field across each element, cross sectional slice of the yz plane down the center of the vessel.

In the semi-baffled system, the impeller clearance is adjusted to 100 mm using the MRF approach. The Newton number remains fairly constant at approximately 0.631, slightly increased from the impeller clearance set at 40 mm, which gave 0.627. Details of the data and velocity profile are presented in Table 4.6 below. Figure 4.14 indicates that using the MRF approach without surface deformation results in a linear result across

various impeller speeds. Figure 4.15 depicts the normalized velocity flow fields across each grid element.

Table 4.6 Newton Numbers for the Semi-baffled System, H/T = 1

Agitation Rate Ni (RPM)	Reynolds Number Re	Torque M (N·m)	Power P (W)	Newton Number Np
20	1.38E+04	0.00380	0.008	0.631
50	3.44E+04	0.0237	0.124	0.630
75	5.16E+04	0.0534	0.419	0.631
100	6.88E+04	0.0952	0.996	0.632
150	1.03E+05	0.214	3.363	0.632
200	1.38E+05	0.380	7.959	0.631

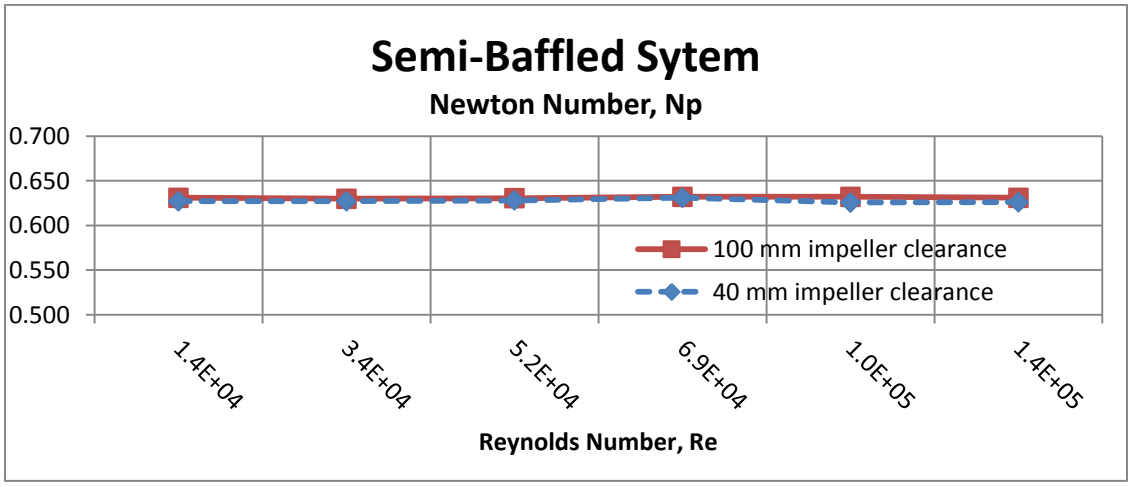

Figure 4.14 Newton numbers, semi-baffled, H/T=1, varying impeller clearance.

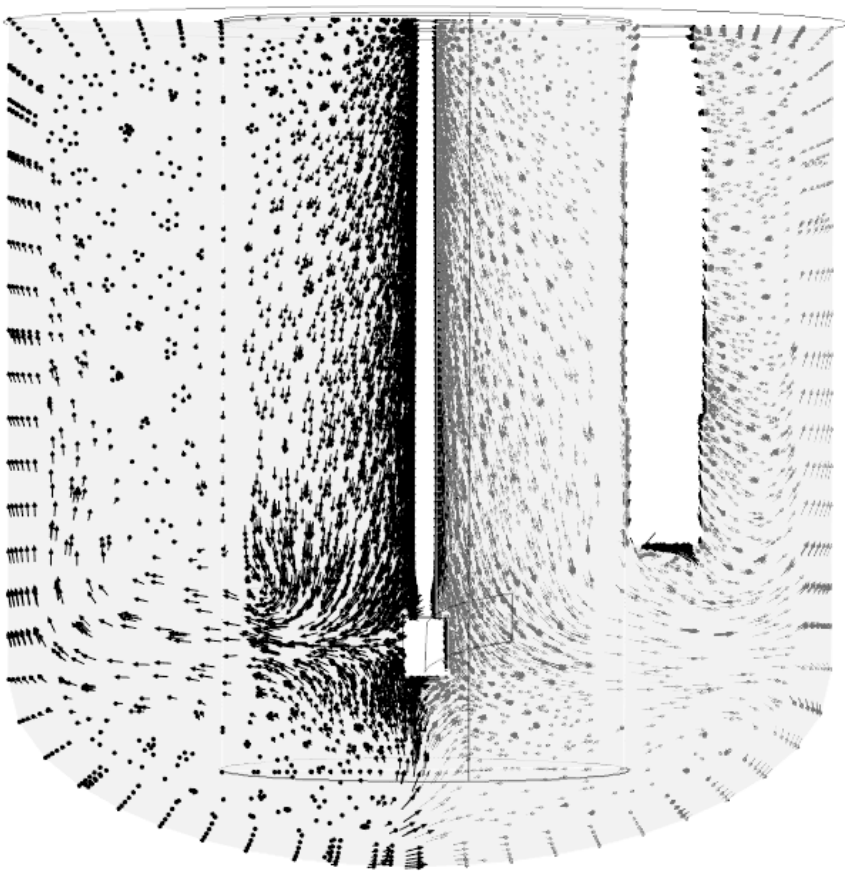

Figure 4.15 Velocity profile of the semi-baffled system, side view, 100 mm clearance, 100 RPM, normalized vector flow field across each element, cross sectional slice of the yz plane down the center of the vessel.

4.3 Vortex Formation with Time Dependent Study

Conditions are added for the modelling of surface deformation in the un-baffled system. The rotational speed is considered at 100 RPM and 200 RPM. Liquid level is set equal to tank diameter at 445 mm. The full vessel height is considered in the geometry to emphasize the slip condition applied to the inner walls. Impeller clearance is 100 mm. Prior to running the model, an initial solution is calculated using the MRF approach. The time dependent study is carried out using the Sliding Mesh approach with the reduced, submerged rotating domain and unstructured, adaptive stationary domain. Viscous

stresses are applied at the surface using Equation 3.5. The system is run over the course of 6 seconds in 0.1 second intervals. At 6 seconds, vortex depth is measured from the bottommost point of the vortex to the original liquid height, giving 0.102 m at 100 RPM and 0.228 m at 200 RPM. Figures 4.16, 4.17, and 4.18 reveal the simulated vortex formation. Results suggest that CFD can be utilized as an effective tool to simulate vortex formation to aid the scale-up procedure of industrial-sized bioreactors.

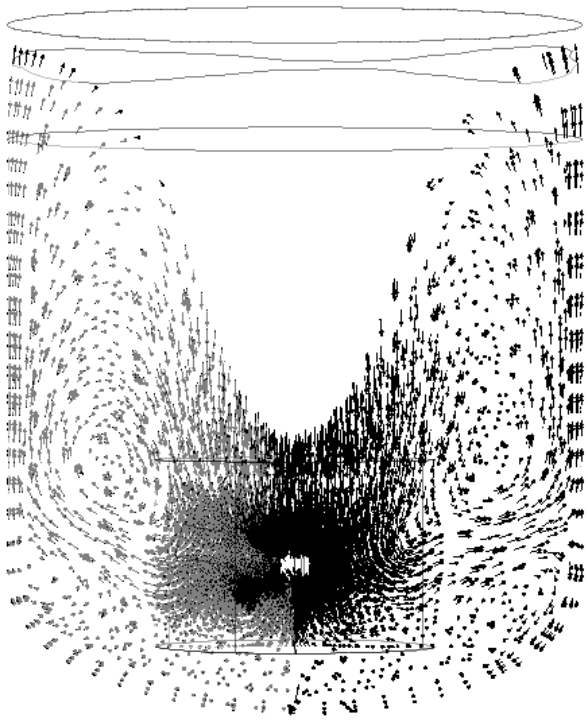

Figure 4.16 Velocity profile, un-baffled system surface deformation, 200 RPM, normalized vector flow field across each element, cross sectional slice of the yz plane down the center of the vessel.

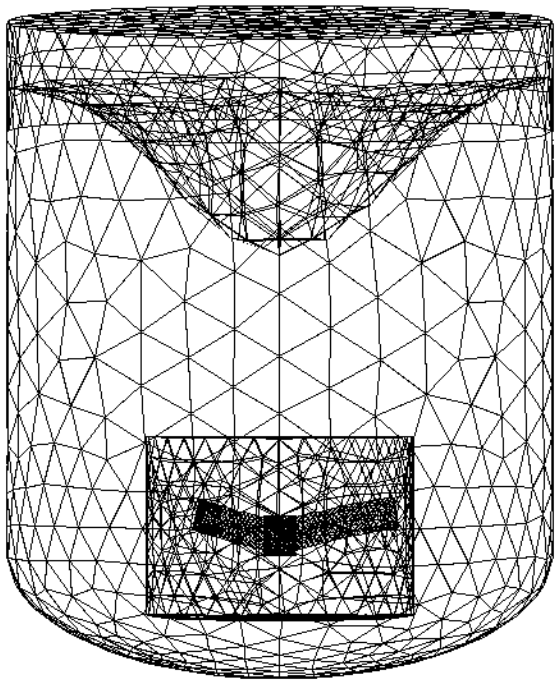

Figure 4.17 Sliding Mesh, un-baffled system, course grid overlay, 100 RPM.

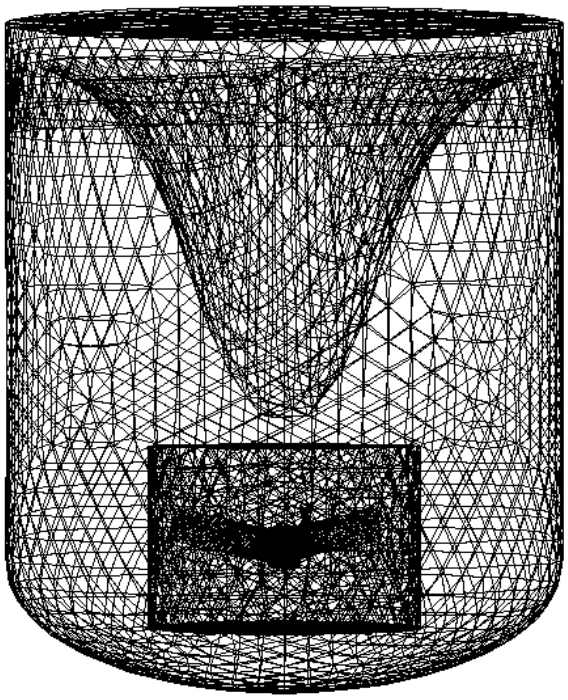

Figure 4.18 Sliding Mesh, un-baffled system, course grid overlay, 200 RPM.

CHAPTER 5

DISCUSSION

5.1 Comparison of Simulation Predictions for Power Number with Previous Experimental Results

Previous studies on power dissipation have been conducted on systems somewhat similar to that studied here [2] [4] [5] [9] [11] [14]. However, the models built and tested in this study are based on an actual scaled down system used in this group [2]. Those experiments were carried out using a 0.25 HP motor for the retreat impeller. Agitation speed and torque were measured using an Interface Rotary Torque Transducer, Model T6 (Dual range 5/0.5 N*m) with a ±0.1 % maximum combined error. The transducer is connected to an Interface Load Cell Indicator, Model 9850 (Digital, Multi-Channel) with a ±0.02 % maximum combined error.

Power dissipation was measured for three separate baffling systems at varying impeller speeds. All agitation speeds produced Reynolds numbers sufficiently high enough to warrant the use of the k-ε Turbulence model. When fully baffled, the CFD simulation using the MRF approach predicted an average Newton number of 0.753, which is very accurate when compared to the experimentally observed 0.764 (averaged over all agitation speeds) [2]. Table 5.1 gives a detailed comparison of the experimental and simulated studies using the MRF approach for each agitation speed and baffling system. There is a noticeable decreasing trend in the power as the baffling is reduced in the simulations. Furthermore, the experimental values show a slight decreasing trend in power as the agitation rate is increased, whereas the CFD study indicates a very stable, linear result across all impeller speeds.

Table 5.1 Comparative Study of the CFD Results to the Experimentally Derived Values, Impeller Clearance = 40 mm, H/T = 1

	Impeller Speed (RPM)			
System	**75**	**100**	**150**	**200**
Fully baffled, experimental	0.838	0.763	0.757	0.724
Fully baffled, CFD Result, MRF	0.757	0.746	0.751	0.751
% Error	-9.68%	-2.23%	-0.79%	3.73%

	Impeller Speed (RPM)			
System	**75**	**100**	**150**	**200**
Un-baffled, experimental	0.355	0.297	0.266	0.295
Un-baffled, CFD Result, SRF	0.311	0.313	0.309	0.310
% Error	-12.4%	5.39%	16.17%	5.08%

	Impeller Speed (RPM)			
System	**75**	**100**	**150**	**200**
Semi-baffled, experimental	0.601	0.547	0.555	0.520
Semi-baffled, CFD Result, MRF	0.631	0.630	0.632	0.631
% Error	5.0%	15.17%	13.87%	21.34%

	Impeller Speed (RPM)
System	**100**
Semi-baffled, experimental	0.547
Semi-baffled, CFD Result, Sliding Mesh	0.532
% Error	-2.74%

MRF is appropriate when vortex formation is minimized with the baffled system. However, the percentage error in semi-baffled systems from Table 4.2 shows that MRF is less adequate in these scenarios and a time dependent study is required for increased accuracy. When the impeller clearance is raised to 200 mm in the fully baffled system,

the CFD model comes very close to the actual value and is also suitable for the MRF approach. This comparison is presented in Table 5.2 below.

Table 5.2 Comparative Study of the CFD results, Impeller Clearance = 200 mm

	Impeller Speed (RPM)			
System	**75**	**100**	**150**	**200**
Fully baffled, experimental	0.751	0.764	0.756	0.759
Fully baffled, CFD Result, MRF	0.816	0.801	0.763	0.726
% Error	8.68%	4.78%	0.89%	-4.32%

The percentage error is reasonably within the same range as the same system at 40 mm clearance. At 40 mm, the impeller was rotating below the baffles, whereas at 200 mm, the impeller flow is alongside the baffle. Therefore, the interaction of the impeller and the baffling is greatly intensified at 200 mm as visualized in Figures 4.10 and 4.13; improving the meshing at the flow continuity boundary between the rotating and stationary domain is likely to produce better results. Furthermore, there is also the possibility of a strong vortex near the surface that is also contributing to the power dissipation [5].

The Sliding Mesh approach was successful in narrowing the percentage error in the semi-baffled system. Using this method, the overall percentage error between the MRF and Sliding Mesh study decreased from -12.4% to -2.74%, an overall increase in accuracy of 9.7%. However, there are limitations to the approach taken in this study. The mesh should be made as refined as computationally feasible at the flow continuity condition to improve the flow fields as they approach the free surface.

Table 5.3 Comparative Study of the CFD results, Including Sliding Mesh, 100 RPM

Semi-Baffled System	Newton Number Np	% Error
Experimental	0.547	n/a
CFD, MRF	0.632	-12.4%
CFD, Sliding Mesh	0.532	-2.74%

5.2 Optimization and Computation Time

Due to the combination of a three blade impeller and either a four plated or single beavertail baffling system, a periodic flow was not considered for this study. Assuming a symmetrical system, such as a four blade impeller with four baffles, the vessel can be divided into equal sections and the system is set to compute only one representative section. For global variables, the value is simply multiplied by the total number of sections to obtain the system value. For demonstration purposes, a sample study was performed on the un-baffled system, where the vessel was divided into three equal sections, one for each of the three impeller blades. After convergence, the Newton number was found to be identical to the value obtained in Section 4.1, but computation time was reduced by over 70%. When sliding mesh or adaptive mesh is not required, adding a periodic flow condition may be sufficient for power dissipation simulations.

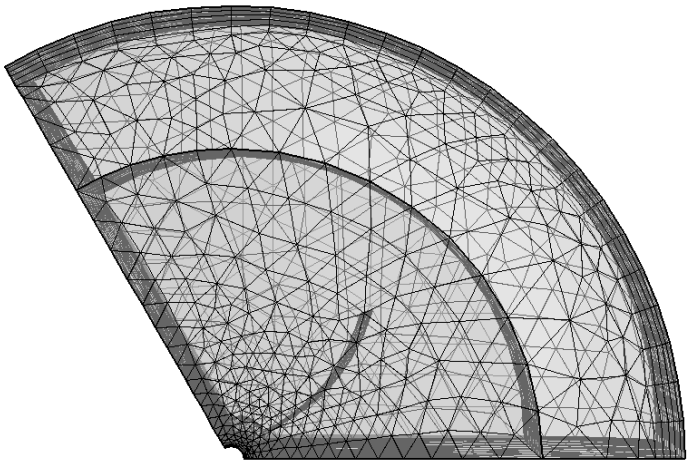

Figure 5.1 Top view, fully-baffled meshing, MRF technique, periodic flow condition.

Additionally, the system is very sensitive to the size of the rotating domain for MRF and Sliding Mesh studies. If the rotating domain boundary is too close to the impeller blade tips, the system may over-estimate the torque; too far away and the system may under-estimate torque or even fail to converge. Geometries should be simplified to avoid inverted meshing and edges should be smoothed where appropriate.

CHAPTER 6

CONCLUSIONS

From the modeling work presented in this study, several conclusions may be drawn about the CFD simulation of the mixing system studied here. The Multiple Reference Frame approach is appropriate for scenarios where surface deformation does not become an issue (i.e., fully baffled systems). In the fully baffled system, the power dissipation was in very close agreement with the experimental results. At the agitation rates considered in this study, the Reynolds number was sufficiently high enough that the inertial forces dominated the viscous forces. Therefore, the power became proportional to the Reynolds number; consequently, the Newton number essentially remained constant for each impeller speed. Overall, the Newton number of the three blade retreat impeller in fully baffled conditions where H/T =1 was calculated at approximately 0.75, consistent with the experimental result and also in published literature.

In the un-baffled system, the SRF was appropriate to describe the power requirements of the system. The Froude number becomes a considerable dynamic beyond a Reynolds Number of 200 where vortex formation is associated with a decrease in power dissipation. The impact of inertial forces is simulated with the application of centrifugal and Coriolis effects. Accuracy is achieved without performing time dependent studies. At H/T =1, 100 RPM, and Re = 6.88E04, the Newton number is calculated as 0.313 and in agreement with experimental value. For the purposes of modeling the actual vortex, three conditions were added to the model: submerge the rotating domain so that it is encapsulated within a stationary domain, apply a free surface

condition that allows for deformation of the grid within the stationary domain, and allow slippage on the interior portion of the vessel walls. Running the model with these additions revealed a large central vortex consistent with expectations.

By increasing the impeller clearance, a noticeable difference in the flow pattern emerges, as evidenced by Figures 4.10 and 4.13. Furthermore, the increased impeller clearance also increases the flow interaction between the impeller and baffling, further changing the velocity profile of the system. These two changes drive a minor increase in Newton number which is consistent with the experimental value. Also, changes to the velocity profile closer to the liquid surface suggest that the solution is not truly steady state, but it may produce acceptable approximations. A best practice would be to utilize the results from the approximation and set it as the initial solution of a time dependent study in order to fully model the unsteady solution of at least one full rotation.

This work reveals that CFD is capable of modeling and reproducing similar results as those recorded from the physical experiments. Steady state approximations can be utilized to calculate global variables with accuracy in baffled systems. Further research could be conducted by refining the meshing around the impeller and also recalculating the time dependent study at increasing impeller speeds in order to demonstrate a decreasing trend in the Newton number for semi-baffled and un-baffled systems.

APPENDIX A

SYSTEM GEOMETRY SPECIFICATIONS

Appendix A contains the values utilized in the geometry construction.

Table A.1 Geometry Specifications

Variable	Value	Description
VesselDiam	445 mm	vessel diameter
LiquidHeight	VesselDiam	liquid height
VesselHeightBottomToFlat	101.6 mm	vessel height from bottom to flat section
VesselHeightFromFlat	LiquidHeight-VesselHeightBottomToFlat	vessel height from flat section
ImpDiam	101.29 mm	impeller total diameter
ImpShaftDiam	12.7 mm	impeller shaft diameter
ImpShaftHeight	470 mm	impeller shaft height
ImpSpeed	1.25 1/s	impeller rotational speed
ImpBottomClearance	100 mm	impeller bottom clearance
RetreatImpBladeThickness	12.7 mm	retreat impeller blade thickness
RetreatImpConnShaftDiam	25.5 mm	retreat impeller connecting shaft diameter
RetreatImpBladeHeight	25.4 mm	retreat impeller blade height
RetreatImpBladeRadOfCurve	91.7 mm	retreat impeller blade radius of curvature
RetreatImpBladeCurveCentralAngle	62.2 deg	retreat impeller blade curve central angle
RetreatImpConnShaftHeight	31.9 mm	retreat impeller connecting shaft height
RetreatImpShaftOffset	3.08 mm	retreat impeller shaft offset
RetreatImpBladeAngle	15 deg	retreat impeller blade angle
BaffleOffsetFromWall	70.3 mm	baffle offset from vessel wall
BaffleOffsetFromBottom	170 mm	baffle offset from vessel bottom
BeaverBaffleBottomDiam	40.12 mm	beavertail baffle bottom diameter
BeaverBaffleBottomLength	67.7 mm	beavertail baffle bottom length
BeaverBaffleMidDiam	44.6 mm	beavertail baffle middle diameter
BeaverBaffleMidLength	152.4 mm	beavertail baffle middle length
BeaverBaffleTopDiam	30.5 mm	beavertail baffle top diameter
BeaverBaffleTopaLength	225 mm	beavertail baffle top length
BeaverBaffleThickness	27.6 mm	beavertail baffle thickness
BeaverBaffleConeHeight	46 mm	beavertail baffle cone section height
PlateBaffleWidth	45 mm	plate baffle width
PlateBaffleThickness	4.76 mm	plate baffle thickness
PlateBaffleHeight	445 mm	plate baffle height

APPENDIX B

TECHNICAL INFORMATION OF THE COMPUTATIONAL HARDWARE AND SOFTWARE USED IN THIS WORK

Appendix B contains the computer and software information utilized in this study.

Component	Description
Operating System	Windows 7 Professional, 64 bit, Service Pack 1, Microsoft Corporation
Processor	AMD Phenom 9950 Quad-Core Processor, 2.60 GHz
RAM	8 GB 240-Pin DDR2 SDRAM 1066
Graphics	EVGA GeForce GT 630, 2 GB DDR3
Computing Software	COMSOL Multiphysics 4.4 with CFD Module

Figure A.1 Computer technical information.

APPENDIX C

TIME DEPENDENT STUDY DATA

Appendix C contains the data from the time dependent study performed on the semi-baffled system.

Table A.2 Time Dependent Study Data, Semi-baffled System

Semi-baffled system, Sliding Mesh Technique
H/T =1, 100 RPM, Re = 6.88E-04

Time (s)	Revolutions	Power (W)
0	-	0.000
1	1.67	0.965
2	3.33	1.004
3	5.00	0.939
4	6.67	0.895
5	8.33	0.878
6	10.00	0.866
7	11.67	0.861
8	13.33	0.855
9	15.00	0.851
10	16.67	0.844
11	18.33	0.837
12	20.00	0.829
13	21.67	0.818
14	23.33	0.811
15	25.00	0.806
16	26.67	0.807
17	28.33	0.809
18	30.00	0.812
19	31.67	0.816
20	33.33	0.821
21	35.00	0.824
22	36.67	0.826
23	38.33	0.827
24	40.00	0.828
25	41.67	0.828
26	43.33	0.828
27	45.00	0.827
28	46.67	0.827
29	48.33	0.826
30	50.00	0.826
31	51.67	0.826
32	53.33	0.827
33	55.00	0.826

REFERENCES

1. Anderson, J.D. (1995). *Computational fluid dynamics: The basics with applications*. 1st Ed., pp. 1-212. New York, NY: McGraw-Hill.

2. Banerjee, A. (2013). *Power dissipation and mixing time in a partially filled pharmaceutical reactor equipped with a retreat-blade impeller at different fill ratios*. MS Thesis, Otto H. York Department of Chemical, Biological and Pharmaceutical Engineering, New Jersey Institute of Technology, Newark, NJ.

3. Bronshtein, I.N., Semendyayev, K.A., Musiol, G., & Mühlig, H. (2007). *Handbook of mathematics*. 5th Ed., p. 140. New York, NY: Springer.

4. Campolo, M., & Soldati, A. (2002). Appraisal of fluid dynamic efficiency of retreated-blade and turbofoil impellers in industrial-size CSTRs. *Industrial & Engineering Chemistry Research*, 41 (5), 1370-1377.

5. Cartland Glover, G.M., & Fitzpatrick, J.J. (2007). Modelling vortex formation in an unbaffled stirred tank reactors. *Chemical Engineering Journal*, 127 (1), 11-22.

6. Dickey, D.S., Bittorf, K.J., Ramsey, C.J., & Johnson, K.E. (2004). Understand flow patterns in glass-lined reactors. *Chemical Engineering Progress*, 100 (11), 21-25.

7. Doran, P.M. (2013). *Bioprocess engineering principles*. 2nd Ed., pp. 201-285. New York, NY: Academic Press.

8. Geankoplis, C.J. (2003). *Transport processes and separation process principles*. 4th Ed., pp. 154-162. Upper Saddle River, NJ: Prentice Hall.

9. Lia, M., Whitea, G., Wilkinsona, D., & Roberts, K.J. (2005). Scale up study of retreat curve impeller stirred tanks using LDA measurements and CFD simulation. *Chemical Engineering Journal*, 108 (2), 81-90.

10. McCabe, W.L., Smith, J.C., & Harriott, P. (2004). *Unit operations of chemical engineering*. 7th Ed., pp. 244-265. New York, NY: McGraw-Hill.

11. Nagata, S. (1975). *Mixing principles and applications*. New York, NY: John Wiley & Sons, Inc.

12. Paul, E.L., Atiemo-Obeng, V.A., Kresta, S.M., & North American Mixing Forum. (2004). *Handbook of industrial mixing: Science and practice*. Hoboken, NJ: John Wiley & Sons, Inc.

13. Reynolds, W.C. (1976). Computation of turbulent flows. *Annual Review of Fluid Mechanics*, 8, 183-208.

14. Santos-Moreau, V., Brunet-Errard, L., & Rolland, M. (2012). Numerical CFD simulation of a batch stirred tank reactor with stationary catalytic basket. *Chemical Engineering Journal*, 207-208 (1), 596–606.

15. Seader, J.D., & Henley, E.J. (1998). *Separation process principles*. 1st Ed., pp. 1-50. New York, NY: John Wiley & Sons, Inc.

16. Thangam, S., & Institute for Computer Applications in Science and Engineering. (1991). *Analysis of two-equation turbulence models for recirculating flows*, 61 (91), 1-20. Hampton, VA: ICASE & National Aeronautics and Space Administration Langley Research Center.